

UNCLASSIFIED

AD NUMBER
AD231112
NEW LIMITATION CHANGE
TO Approved for public release, distribution unlimited
FROM Distribution authorized to U.S. Gov't. agencies and their contractors; Administrative/Operational Use; JAN 1958. Other requests shall be referred to US Naval Ordnance Lab., White Oak, Silver Spring, MD.
AUTHORITY
US Naval Ordnance Lab ltr dtd 29 Aug 1974

THIS PAGE IS UNCLASSIFIED

UNCLASSIFIED

AD

231112

FOR
MICRO-CARD
CONTROL ONLY

1 OF 1

Reproduced by

Armed Services Technical Information Agency

ARLINGTON HALL STATION; ARLINGTON 12 VIRGINIA

UNCLASSIFIED

"NOTICE: When Government or other drawings, specifications or other data are used for any purpose other than in connection with a definitely related Government procurement operation, the U.S. Government thereby incurs no responsibility, nor any obligation whatsoever; and the fact that the Government may have formulated, furnished, or in any way supplied the said drawings, specifications or other data is not to be regarded by implication or otherwise as in any manner licensing the holder or any other person or corporation, or conveying any rights or permission to manufacture, use or sell any patented invention that may in any way be related thereto.

ADM 33112

ADJ. FILE CO.

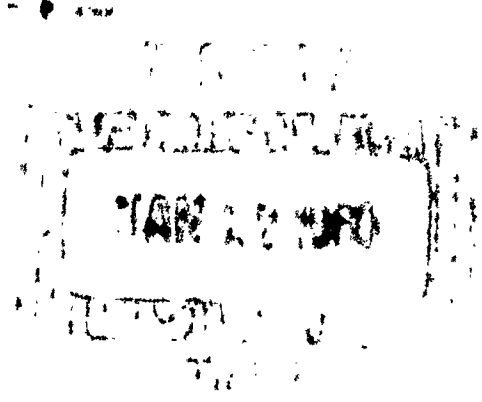
NAVORD REPORT

5668

WAKE INVESTIGATION ON SHARP AND BLUNT NOSE CONES AT SUPERSONIC SPEEDS (U)

FC

28 JANUARY 1958



U. S. NAVAL ORDNANCE LABORATORY
WHITE OAK, MARYLAND

**Best
Available
Copy**

NAVORD Report 5668

Aerodynamics Research Report 8

WAKE INVESTIGATION ON SHARP AND BLUNT NOSE
CONES AT SUPERSONIC SPEEDS

Prepared by:

R. Lehnert
V. L. Schermerhorn

ABSTRACT: A study was made of the relationships between given local flow conditions at the downstream end of cones in supersonic flow and the corresponding base pressure and wake configuration.

The models chosen for this investigation were a 10° semi-apex angle, sharp cone and a 10° semi-apex angle, sphere cone.

Surface pressure distribution and base pressure measurements were made as well as total-pressure surveys of the wake and the boundary-layer near the base. All of the measurements were taken at zero angle of attack. Variation of the boundary-layer profiles immediately upstream of the cone bases was accomplished by changing surface roughness and the wind-tunnel supply pressure and temperature. The local Mach number was the same at the downstream end of both cone models due to the proper choice of the ambient Mach number.

The boundary-layer development along the cone surfaces was calculated for each case tested in the wind tunnel. The momentum thickness Reynolds numbers at the end of the cones derived from these calculations were in good agreement with the ones obtained from the boundary-layer surveys.

It was established that the base pressure and the wake angle are the same for sharp and blunt nose cones of the same half angle when the local Mach number and the Reynolds number based on boundary-layer momentum thickness at the downstream end of the cones are the same.

U. S. NAVAL ORDNANCE LABORATORY
White Oak, Silver Spring, Maryland

This report presents results of experimental wake-flow studies on sharp and spherical-nose 10° semi-apex angle cones and the correlation between wake flow behavior and local flow conditions at the downstream end of the cone. Further, a theoretical study of the boundary-layer development along the cone surfaces was carried out.

The task objective was originated by Dr. R. K. Lobb and the work was performed for the Army Ballistics Missile Agency under Task Number NOL-300.

The authors are deeply indebted to Dr. R. K. Lobb for his active interest in this project. Particular acknowledgement and thanks are due to Mr. J. Persh who participated in the theoretical boundary-layer treatment as a consultant and promoted greatly the IBM machine computations. Further, the authors are indebted to many persons too numerous to mention in the Aerodynamics and Mathematics Departments for various contributions to model and instrumentation design and fabrication, wind-tunnel testing, and data evaluation. However, Mr. Henry Sweet is to be particularly commended for the excellent manner in which he handled the complex test set ups and the wind-tunnel operation associated with the project. Thanks are due W. R. Witt, Jr. and J. J. Brady for the use of shadographs taken in the NOL Pressurized Ballistics Range.

MELL A PETERSON
Captain, USN
Commander

R. KENNETH LOBB
By direction

NAVORD Report 5668

CONTENTS

	Page
INTRODUCTION.....	1
DESCRIPTION OF FACILITY, MODELS, AND TECHNIQUES.....	1
APPLICATION OF BOUNDARY-LAYER THEORY.....	3
RESULTS AND DISCUSSIONS.....	4
Surface Pressure Distribution.....	4
Boundary-Layer Characteristics and Momentum Thickness Reynolds Number.....	5
Base Pressure as a Function of $Re_{\theta,c}$	7
Wake Angle as a Function of $Re_{\theta,c}$	8
Effect of Base Shape on Base Pressure and Wake Angle.....	9
Base Pressure Distribution on a Spherical Base Cone.....	10
CONCLUDING REMARKS.....	10
REFERENCES.....	11
TABLE I Orifice Locations	
APPENDIX A: CALCULATION OF THE BOUNDARY-LAYER DEVELOPMENT ALONG THE CONE SURFACES	
APPENDIX B: EFFECTS OF SURFACE ROUGHNESS	

NAVORD Report 5668

ILLUSTRATIONS

- Figure 1 10° Sharp Cone with Mounting Sting
 Figure 2 10° Sphere Cone with Mounting Sting
 Figure 3 10° Sphere Cone with Spherical Base and Mounting Sting
 Figure 4 Diagram of Orifice Locations and Single Roughness Elements
 Figure 5 10° Sphere Cone with No. 24 Grain Distributed Surface Roughness Mounted in the Wind Tunnel Test Section
 Figure 6 Surface Pressure Distribution on the 10° Sphere Cone at $Ma_{\infty} = 4.74$
 Figure 7 Momentum Thickness Reynolds Number as a Function of Free-Stream Reynolds Number per Foot
 Figure 8 Spark Schlieren Photographs of the 10° Sharp Cone
 Figure 9 Momentum Thickness Reynolds Number Distribution on the 10° Sharp Cone, $Ma_{\infty} = 2.74$, 125 Micro-inch Finish
 Figure 10 Momentum Thickness as a Function of Distance Along Model Surface in Terms of Reynolds Number
 Figure 11 Base Pressure Ratio of the 10° Sharp Cone and the 10° Sphere Cone as a Function of $Re_{\theta,c}$
 Figure 12 Schlieren Photograph (1/100 sec) of the 10° Sharp Cone at $Ma_{\infty} = 2.76$ and $Re_{\theta,c} = 2470$
 Figure 13 Total Pressure Wake Profile for the 10° Sphere Cone
 Figure 14 Wake Angle of 10° Sharp Cone and 10° Sphere Cone as a Function of $Re_{\theta,c}$
 Figure 15 Shadowgraph of a 10° Semivertex Angle Cone at $Ma_{\infty} = 2.35$
 Figure 16 Base Pressure Distribution on the Rough 10° Sphere Cone with Spherical Base at $Ma_{\infty} = 4.74$
 Figure A1 Location of the End of Transition as a Function of Supply Pressure for the Rough 10° Sphere Cone
 Figure A2 Location of the End of Transition as a Function of Supply Pressure for the 10° Sharp Cone
 Figure A3 Local Skin Friction Coefficient as a Function of Re_{θ} for 10° Sharp Cone
 Figure A4 Results of Measurements on Regular Roughness Patterns (Ref. 1)
 Figure A5 Reynolds Number, $Re_{\theta,c}$, as a Function of Supply Pressure, P_s , for the 10° Sharp Cone
 Figure A6 Reynolds Number, $Re_{\theta,c}$, as a Function of Supply Pressure for the 10° Sphere Cone
 Figure B1 Effect of Surface Roughness on Base Pressure

NAVORD Report 5668

SYMBOLS USED IN TEXT

C_f	local skin friction coefficient
d	distance between roughness elements
D	base diameter of roughness elements
H	shape parameter = $\frac{\delta^*}{\theta}$
k	average roughness elevation
k_s	equivalent sand roughness
L	axial length
Ma	Mach number
P	static pressure
P_o'	Pitot pressure
r	recovery factor
R	base radius
Re/Ft	Free-stream Reynolds number per foot; $Re/Ft = \frac{U_\infty \rho_\infty}{\mu_\infty}$
Re_θ	Reynolds number based on boundary-layer momentum thickness or Momentum thickness Reynolds number $Re_\theta = \frac{U_e \rho_e \theta}{\mu_e}$
$Re_{\theta,c}$	Re_θ at the downstream end of the cone
Re_s	Reynolds number based on distance along surface from stagnation point; $Re_s = \frac{U_e \rho_e s}{\mu_e}$
s	contour length from stagnation point (see Figure 6)
T	absolute temperature
T_o'	stagnation temperature
U	velocity in flow direction
Y	model contour ordinate (see Table I)
α	angle between a surface element and the flow direction ahead of the bow shock
β	angle of elevation (see Figure 4)
γ	ratio of specific heats
δ^*	boundary-layer displacement thickness

NAVORD Report 5668

ϵ	wake angle (see Figure 12)
θ	boundary-layer momentum thickness
μ	viscosity
ν	kinematic viscosity
ρ	density
ψ	azimuth angle (see Figure 4)

The symbols $a, b, c, d, e, \ell, s_w, n, \bar{n}, \omega$ are empirical constants and are defined in place in Appendix A

SUBSCRIPTS

ad	equilibrium wall temperature for zero heat transfer
b	values on base or sting
B	values inside the boundary layer
c	values on cone at most downstream station (1.5 inches upstream of base)
e	values at outer edge of boundary layer
inc	incompressible
L	value at edge of laminar sub-layer
Lam	laminar
o	supply conditions
R	rough surface
s	distance from nose on model contour
TR	transition values
Turb	turbulent values
w	values in the wake
∞	undisturbed free-stream conditions

WAKE INVESTIGATION ON SHARP AND BLUNT NOSE
CONES AT SUPERSONIC SPEEDS

INTRODUCTION

1. The wake of supersonic vehicles is known to be dependent upon the local-flow characteristics directly upstream of the base (references (a), (b), and (c)). Consequently, for a given body geometry, knowledge of the structure of the boundary-layer as well as the Mach number at this critical locale constitutes the key for predicting the wake-flow. The common similarity parameters, Mach number and Reynolds number based on free-stream conditions, do not correlate in a unique fashion the pertinent local flow conditions with wake-flow structure.
2. A study was made at the Naval Ordnance Laboratory, White Oak, to establish experimentally whether or not a unique relationship exists between given local-flow conditions at the downstream end of cones in supersonic flow and the resulting wake conditions independent of the history of the generation of these local conditions.
3. The models chosen for this investigation were a 10° semi-apex angle, sharp-nose cone and a 10° semi-apex angle, spherical nose cone, being referred to later on also as the sharp cone and the blunt cone, respectively.
4. Local-flow characteristics at the most downstream station on the cones were determined from surface pressure distribution measurements, wall temperature measurements, and boundary-layer total pressure surveys. Base pressures were measured and the corresponding wake-flow structures were obtained from total-pressure wake surveys, schlieren photographs, and Prandtl-Meyer expansion computations. The sharp cone was tested at Mach numbers of 2.66, 2.74, and 2.76 while the blunt cone data were taken at Mach numbers of 4.74 and 4.85. Boundary-layer surveys were made for a restricted number of tests; consequently, it was necessary to calculate the boundary-layer growth along the body contours in order to have a momentum thickness Reynolds number, $Re_{\theta,c}$ with which to correlate the wake angles and base pressures of all the tests.

DESCRIPTION OF FACILITY, MODELS, AND TECHNIQUES

5. The experimental investigation was performed in the NOI. 40 x 40 cm continuous Aeroballistics Tunnel No. 2. This supersonic, recirculating type tunnel is capable of continuous operation in a Mach number range from 1.2 to 5.0 at supply pressures from about 0.2 to 3.5 atmospheres and at supply temperatures from 300°K to 400°K .

NAVORD Report 5668

6. The models used for this investigation were a 10° semi-apex angle, sharp-nose cone (sharp cone) with a flat base of 6 inches in diameter (Figure 1) and a 10° semi-apex angle, sphere cone (blunt cone) with the same base diameter (Figure 2). The sphere cone nose radius was 1.5 inches or 0.5 times the base radius (R) giving the sphere cone a bluntness ratio of 0.5 R while the sharp cone nose radius was 0.005 inches. In addition, the flat base could be exchanged for a spherical base with a radius of 4.618 inches (Figure 3).

7. The distribution and location of the 16 static pressure orifices on the nose and the conical surface of the blunt cone are shown in Figure 4 and in Table I. The sharp cone was fitted only with orifices at stations 14, 15, and 16 located 1.5 inches upstream of the base.

8. Base pressure taps, were distributed over the spherical base as indicated in Figure 4 and Table I and on the support sting at its intersection with either the flat or the spherical base as shown in Figure 4.

9. A thermocouple was placed 1.5 inches upstream of the base of the sharp cone for measuring wall temperatures.

10. The original surface finish of both models was about 125 micro-inches. During the investigation the sharp cone surface was polished to a finish of 15 micro-inches in an effort to obtain data at lower Reynolds numbers. To trip the boundary-layer on the blunt cone single roughness elements in the form of various diameter annular trip rings, inserted at the junction of the nose section and the conical body (Figure 4) were first used and secondly a distributed surface roughness of No. 24 grain carborundum powder (Figure 5) was applied.

11. The models were mounted in the NOL 40 x 40 cm Continuous Aeroballistics Tunnel No. 2 on a cylindrical sting support 1.5 inches in diameter. At its downstream end, the sting was fastened to the tunnel sidewall by a special double-wedge support beam. A hinge system at that location permitted a pitch-and-yaw angle adjustment of the models while the tunnel was blowing. The desired zero pitch-and-yaw attitude was achieved when the differential pressures between the three cone surface orifices near the base were zero within the measuring accuracy (0.05 mm Hg).

12. For the surface and base pressure distribution measurements, multiple manometer banks with mercury and Dow Corning Silicone oil (DC200 of a kinematic viscosity of 10 centistokes) were employed. These manometer banks were developed at NOL and their features are described in reference (d).

NAVORD Report 5668

13. Wake surveys were performed with a total pressure probe at stations two inches and four inches downstream of the model bases. An NOL precision manometer was used to make the measurements. Assuming the wake flow to be axially symmetrical, the wake studies were restricted to radial surveys in a vertical plane only, covering a distance from the support sting surface to a region well outside the mixing zone of the wake.

14. Boundary-layer profiles in a vertical plane were measured on the cone 0.9 inch upstream of the base with a total pressure probe.

15. The wake and the boundary-layer total pressure surveys were made with the same probe. The probe nose had a wall thickness of 0.003 inch and an opening of 0.078 inch by 0.002 inch. Support and drive of the probe were accomplished by the use of a three-directional micro-drive apparatus. With this arrangement the locations of the probe nose were determined with an accuracy of ± 0.002 inch. The starting position for all surveys was given by the mechanical contact of the probe nose with either the model-support sting surface or the cone surface. This position was determined with a precision cathetometer to 0.0004 inch. Due to the finite wall thickness of the probe nose the survey station nearest to any surface was restricted to a distance of 0.004 inch. The survey intervals were varied in an individual fashion as dictated by the minimum number of data points needed for plotting a wake or boundary-layer profile.

16. Spark-schlieren photographs for the determination of boundary-layer transition were taken at each run. The exposure time was in the order of one micro second. Schlieren photographs with 1/100 second exposure time were also taken. They showed the average wake-flow shapes.

17. The sharp cone was tested at Mach numbers of 2.66, 2.74, and 2.76 at supply pressures from 0.4 atmosphere to 1.6 atmospheres and at supply temperatures from 39°C to 58°C. Blunt cone tests were conducted at Mach numbers of 4.74 and 4.85 with a variation of supply pressures from one atmosphere to 3.5 atmospheres and supply temperatures from 30°C to 55°C.

APPLICATION OF BOUNDARY-LAYER THEORY

18. For studying the interrelationship between boundary-layer behavior and wake-flow, the Reynolds number based on the boundary-layer momentum thickness, $Re_{\theta, c}$, was chosen to describe the boundary-layer at the base. The simplifying assumption of zero heat transfer was made.

NAVORD Report 5668

19. Measurements of the boundary-layer profiles needed for the $Re_{\theta,c}$ determinations were carried out for some of the tests. Theoretical calculations of the boundary-layer development along the body contour were made in order to determine $Re_{\theta,c}$ for all the tests for which there were no experimental boundary-layer data.

20. The method used for the calculation of the boundary-layer growth is a stepwise solution of the boundary-layer momentum equation for compressible flow:

$$\frac{d\theta}{ds} = \frac{C_f}{2} - \theta \left[\frac{(\delta^*/\theta)+2}{U_e} \frac{dU_e}{ds} + \frac{1}{\rho_e} \frac{d\rho_e}{ds} + \frac{1}{Y} \frac{dY}{ds} \right] \quad (1)$$

using appropriate values of C_f and δ^*/θ throughout the laminar, transition, and turbulent regions of the boundary-layer (references f, h, j). The quantities U_e , ρ_e , Y and their derivatives and the temperatures T_{ad} and T_e were determined from the measured pressure distribution (Figure 6), ambient flow data, and the model geometry. Details of the calculation procedure are given in Appendix A.

RESULTS AND DISCUSSIONS

Surface Pressure Distribution

21. The results of the pressure distribution measurements on the blunt cone with a 125 micro inch finish at $Ma_\infty = 4.74$ are given in the form of $p/p_0 = f(s/R)$ in Figure 6 and comparison is made with theory. The pressure distribution over the spherical part of the model has been calculated according to the modified Newtonian approach:

$$\frac{p - p_\infty}{p_0 - p_\infty} = \sin^2 \alpha \quad (2)$$

where α is the angle between a surface element and the flow direction ahead of the bow shock. The pressure on the cone surface as determined from the Kopal tables (reference (e)) is also given for comparison.

22. Because of the deviation between the Newtonian distribution and the experimental data only the experimental pressure distribution has been used for the computation of the pressure gradients needed for the calculation of the boundary-layer development and the Reynolds numbers based on the momentum thickness of the boundary layer.

NAVORD Report 5668

23. From the data obtained at stations 14, 15, and 16, (1.5 inches upstream of the base) the local Mach number was determined to $Ma_c = 2.46$.

24. An evenly distributed roughness (No. 24 grain carborundum powder) did not affect the surface pressure distribution.

Boundary-Layer Characteristics and Momentum Thickness Reynolds Number.

25. Boundary-layer velocity profiles, momentum thickness, and momentum thickness Reynolds numbers just upstream of the cone base have been determined from the boundary-layer total pressure surveys, the measured local static pressure and a calculated boundary-layer temperature profile. In this evaluation the usual assumption was made that the static pressure across the boundary-layer is constant and is equal to the pressure measured on the cone surface. Local wall temperature data on the sharp cone at $Ma_\infty = 2.76$ were found to be in agreement with adiabatic recovery temperatures. Therefore, the wall temperatures for all other cases considered were also assumed to be equal to the adiabatic recovery temperatures. The Crocco equation (reference f) was used to determine the temperature profile

$$\frac{T_B}{T_e} = \frac{T_c}{T_e} - \frac{T_c - T_{ad}}{T_e} \left(\frac{U_B}{U_e} \right) - \frac{T_{ad} - T_e}{T_e} \left(\frac{U_B}{U_e} \right)^2 \quad (3)$$

With

$$\frac{T_c}{T_e} = \frac{T_{ad}}{T_e} = 1 + r \frac{\gamma-1}{2} Ma_e^2, \text{ where the recovery factor } r$$

was assumed as 0.850 for the laminar region, 0.870 for the transitional region and 0.896 in the turbulent region, equation (3) reduces to

$$\frac{T_B}{T_e} = \frac{T_{ad}}{T_e} + \left(1 - \frac{T_{ad}}{T_e} \right) \left(\frac{U_B}{U_e} \right)^2 \quad (4)$$

where:

$$\left(\frac{U_B}{U_e} \right)^2 = \frac{Ma_B^2}{Ma_e^2} \frac{T_B}{T_e} \quad (5)$$

NAVORD Report 5668

Solving equations (4) and (5) together yields

$$\frac{T_e}{T_B} = \frac{T_e}{T_{ad}} + \frac{Ma_B^2}{Ma_e^2} - \frac{Ma_B^2}{Ma_e^2} \frac{T_e}{T_{ad}} \quad (6)$$

which was used with equation (5) to determine θ from:

$$\theta = \int_0^{\delta} \frac{T_e}{T_B} \frac{U_B}{U_e} \left(1 - \frac{U_B}{U_e}\right) dY \quad (7)$$

The Reynolds number based on the boundary-layer momentum thickness is then determined by

$$Re_{\theta} = \rho_e U_e \frac{\theta}{\mu_e} \quad (8)$$

or specifically - as needed for the correlation of base pressure and wake angle - at the downstream end of the cone by

$$Re_{\theta,c} = \rho_{e,c} U_{e,c} \left(\frac{\theta_c}{\mu_{e,c}}\right) \quad (9)$$

A plot of the momentum thickness Reynolds numbers, $Re_{\theta,c}$, as a function of the free-stream Reynolds numbers per foot, Re/Ft , is given in Figure 7. Because there was reasonable agreement between predicted data and experimental results the theoretically obtained $Re_{\theta,c}$ was used in cases where boundary-layer profiles were not measured. In these cases it was only necessary to have spark schlieren photographs for the determination of the location of the end of transition. Representative samples of these spark schlieren photographs are given in Figures 8(a) and 8(b). The sharp cone with a 15 micro-inch finish at $Ma_{\infty} = 2.76$ and $Re_{\theta,c} = 2470$ shown in Figure 8(a), experienced transition at a free-stream Reynolds number, $Re \approx 4.16 \times 10^6$. At $Ma_{\infty} = 2.74$ and $Re_{\theta,c} = 3090$ (Figure 8(b)) transition on the sharp cone with a surface finish of 125 micro-inches occurred already at a free-stream Reynolds number, $Re \approx 3.45 \times 10^6$. However, in both cases the Reynolds number based on the momentum thickness at the end of transition was the same, $Re_{\theta,TR} \approx 1600$. The corresponding appearance of the end of transition has been pointed out by arrows. The calculated relationship between the momentum thickness Reynolds number and the distance along the surface from the stagnation point at a local Mach number, $Ma_c = 2.50$, is given in Figure 9 for the sharp cone. From this figure

it appears that for the sharp cone the location of the transition region is a function of the supply pressure while in terms of momentum thickness Reynolds number the start of transition occurs at $Re_{\theta} \approx 500$ and the end of transition takes place at $Re_{\theta} \approx 1600$ independent of the supply pressure. A plot of $Re_{\theta,c}$ vs. Re_s for both configurations tested, is given in Figure 10 where both Reynolds numbers are based on the local condition at the edge of the boundary-layer.

Base Pressure as a Function of $Re_{\theta,c}$

26. With the relationship established between $Re_{\theta,c}$ and the Reynolds number per foot (see Figure 7) or $Re_{\theta,c}$ and Re_s (see Figure 10) it was possible to correlate all base pressure data taken with the sharp cone and the blunt cone taking into account model geometry and surface roughness. Figure 11 is a plot of $\frac{P_b}{P_c}$ vs. $Re_{\theta,c}$ where P_b is the base pressure taken at orifices 17 and 18 (Figure 4) one located at the intersection of the flat base and the support sting and the other one 1.0625 inches downstream of the flat base. P_c is the static pressure on the cone surface measured 1.5 inches upstream of the base. Despite the variation of individual parameters known to influence the base pressure (pressure gradient, surface roughness, ambient flow conditions), all the base pressure ratios obtained show a common functional relationship with respect to $Re_{\theta,c}$ when the local Mach number at the end of the cone as well as the base geometry are the same. The previously established general tendency of the base pressure behavior in relation to boundary-layer characteristics (references (a), (b), and (c)) is basically confirmed within the available limits of Reynolds number variation, i.e., (1) rapidly decreasing base pressure ratio with increasing free-stream Reynolds number when the boundary-layer along the entire body surface is apparently laminar; (2) existence of a base pressure ratio minimum when the boundary-layer becomes turbulent at the model base; and (3) slowly increasing base pressure ratio with increasing free-stream Reynolds number approaching a quasi constant value when boundary-layer transition travels upstream on the body. In terms of momentum thickness Reynolds number the onset of boundary-layer transition occurs at $Re_{\theta,c} \approx 500$ where the slope of the $\frac{P_b}{P_c}$ vs. $Re_{\theta,c}$ curve (Figure 11) experiences a sudden change, and the end of transition takes place at $Re_{\theta,c} \approx 1600$ where the base pressure ratio is a minimum.

27. From these results the very interesting conclusion can be drawn that the pressure on the flat base of a cone is a function of the Reynolds number based on the momentum thickness of the boundary-layer at the base for a given Mach number on the cone surface and is independent of the history of the boundary-layer development. In the case of a sufficiently high Reynolds number, $Re_{\theta,c}$, where the boundary-layer at the base is fully turbulent the base pressure seems to be constant with increasing $Re_{\theta,c}$ so that for the $Re_{\theta,c}$ range considered the knowledge of an exact $Re_{\theta,c}$ is no longer necessary. With a turbulent boundary layer the theory of Korst (reference (g)) becomes applicable and comparison with the sharp cone data is made in Figure 11. The agreement between theoretical prediction and experimental data is reasonably good.

Wake Angle as a Function of $Re_{\theta,c}$

28. The wake angle is defined as the angle between the outer edge of the wake mixing zone and the envelope of the displacement-boundary layer (Figure 12). Three different methods were used to determine the wake angle: direct measurement from schlieren photographs, Prandtl-Meyer expansion computation based on measured cone and base pressures, and evaluation of the total pressure profiles measured across the wake. Figure 13 shows a typical example of a total pressure wake profile four inches downstream of the base of the blunt cone at $Ma_{\infty} = 4.74$ and $Re_{\theta,c} = 850$. The wake pressure ratio P_w/P_o' has been plotted as a function of the distance from the support-sting surface, where P_w is the local-total wake pressure, and P_o' is the Pitot pressure measured at the stagnation point of the blunt cone. Between the sting surface and the inner edge of the wake mixing layer P_w/P_o' is constant and at a level corresponding to the pressure measured at the base of the model. Within the mixing layer the pressure rises steeply, the slope of the pressure-distance curve being approximately constant. A sudden deviation from this slope occurs at the outer edge of the mixing layer. The coordinates of the outer edge of the mixing layer, obtained for the various conditions at cross sections two and four inches behind the cone base, were used as the determining coordinates for the wake angle computation.

NAVORD Report 5668

Wake angles obtained by the three different methods have been plotted as a function of $Re_{\theta,c}$ in Figure 14 for the sharp cone and the blunt cone with flat bases. The results show that the wake angle is related to $Re_{\theta,c}$ in a fashion corresponding to the behavior of the base pressure ratio with respect to $Re_{\theta,c}$. It can be noted that the base pressure ratio and wake angle curves demonstrate a perfect mirror image behavior to each other since the wake angle was found to agree with the angle of flow expansion around a sharp corner depending upon the cone and base pressure ratios. This fact is of practical importance for the analysis of shadowgraph and schlieren pictures of models whose base pressures are not known.

29. As an example for the application of this relationship a spark shadowgraph (Figure 15) taken of a smooth 10° semi-apex angle cone (2.88 inch axial length) in the NOL Pressurized Ballistics Range at $Ma_\infty = 2.35$ was evaluated. The wake angles were measured and the cone Mach number was determined as $Ma_c = 2.15$ from the Kopal Tables (reference (e)). With the assumption of a surface roughness equivalent to that of the wind-tunnel model and adiabatic recovery temperature on the model surface a corresponding local Reynolds number Re_s at the end of the cone was computed from the ambient conditions. Using this Re_s and the curve for the sharp cone at $Ma_\infty = 2.74$ ($Ma_c = 2.48$) in Figure 10 an $Re_{\theta,c} = 2620$ was determined. The wake angle plotted in Figure 14 and the corresponding base pressure ratio given in Figure 11 are in good agreement with the wind-tunnel data. Additional evaluations of several other NOL firing range shadowgraphs of 10° cone models at $Ma_\infty = 2.80$ and with a cone Mach number, $Ma_c = 2.50$, yielded a wake angle and a correlated base pressure ratio both being in favorable agreement with the extrapolated wind-tunnel data at $Re_{\theta,c} = 3250$ as shown in Figures 14 and 11, respectively.

Effect of Base Shape on Base Pressure and Wake Angle

30. In addition to the investigations of the two cones with the flat base some base pressure and wake angle data were taken on the rough, blunt cone with a spherical base at $Ma_\infty = 4.74$. This particular configuration was of interest to the sponsoring agency. The data are plotted with the results obtained from the flat base cones in Figures 11 and 14, respectively. It appears that the base pressure ratios and the corresponding wake angles obtained with the spherical base deviate considerably from the flat base data at the lower end of the $Re_{\theta,c}$ region while at about $Re_{\theta,c} = 1700$ the flat and spherical base data are nearly the same.

Base Pressure Distribution on a Spherical Base Cone

31. The base pressure distribution on the spherical base of the blunt 10° sphere cone has been plotted in Figure 16 with $Re_{\theta,c}$ as the parameter. All profiles show the same tendency, namely, that the pressure near the edge is very nearly the same as the one at the sting while a pressure maximum develops in between. The value of $\frac{P_b}{P_c}$ at the edge and the magnitude of the maximum are functions of $Re_{\theta,c}$, i.e., both decrease with increasing $Re_{\theta,c}$.

Concluding Remarks

32. It has been shown that the base pressure and corresponding wake angle of a blunt spherical nose 10° semi-apex-angle cone whose boundary-layer development is subject to pressure gradient and surface roughness effects are the same as those obtained with an ordinary sharp nose 10° semi-apex-angle cone if the momentum thickness Reynolds number and the cone Mach numbers at the base are the same. This finding suggests that base pressure and wake flow data obtained on sharp cones at moderately high free-stream Mach numbers can be applied to blunt cones with the same cone half-angle at higher free-stream Mach numbers.

33. The momentum thickness Reynolds numbers obtained from boundary-layer calculations compared very favorably with those determined from the measured boundary-layer profiles. Consequently, the theoretically predicted Reynolds numbers based on boundary-layer momentum thickness may be used for base pressure and wake angle correlation. In the case of an entirely laminar boundary-layer on the body of a sharp cone no further empirical information is needed for the boundary-layer growth calculation. If transition occurs on the body its location needs to be known for the computation of the transitional and turbulent boundary-layer development.

34. Findings on the relationship between measured wake angles and base pressure ratios established the validity of the application of the Prandtl-Meyer concept to the base pressure problem. Consequently, two of the determining quantities (cone pressure, base pressure, and wake angle) define the third one. This provides the possibility to obtain base pressures fairly well from spark shadowgraphs or schlieren photographs without any pressure measurements, if the model geometry and the ambient flow conditions are known.

NAVORD Report 5668

REFERENCES

- (a) Chapman, Dean R., "An Analysis of Base Pressure at Supersonic Velocities and Comparison with Experiment", NACA TN 2137, 1950
- (b) Kurzweg, H. H., "Interrelationship Between Boundary-Layer and Base Pressure", Journal of Aeronautical Sciences, Vol. 18, No. 11, 1951
- (c) Crocco, L., and Lees, L., "A Mixing Theory for the Interaction Between Dissipative Flows and Nearly Isentropic Streams", Journal of Aeronautical Sciences, Vol. 19, No. 10, 1952
- (d) Kendall, J. M., "Equipment and Techniques for Making Pressure Measurements in Supersonic Wind Tunnels at Mach Numbers up to 5", NAVORD Report 2580, 1952
- (e) Kopal, Z., "Tables of Supersonic Flow Around Cones", Staff of the Computing Section, Technical Report No. 1, MIT, 1947
- (f) Persh, J., "A Procedure for Calculating the Boundary-Layer Development in the Region of Transition from Laminar to Turbulent Flow", NAVORD Report 4438, 1957
- (g) Korst, H. H., Page, R. H., Childs, M. E., "A Theory for Base Pressures in Transonic and Supersonic Flow", University of Illinois, M. E. Technical Note 392-2
- (h) Cohen, C. B., and Reshotko, Eli, "The Compressible Laminar Boundary Layer with Heat Transfer and Arbitrary Pressure Gradient", NACA TN 3326, 1955
- (i) Persh, J., "Hypersonic Missile Aerodynamic Heating Calculations at the Naval Ordnance Laboratory" (Secret), Paper No. 11 presented at the Fourth U. S. Navy Symposium on Aeroballistics, 12, 13, and 14 November 1957
- (j) Persh, J., and Lee, R., "A Method for Calculating Turbulent Boundary-Layer Development in Supersonic and Hypersonic Nozzles Including the Effects of Heat Transfer", NAVORD Report 4200, 1956
- (k) Persh, J., and Lee, R., "Table of Turbulent Boundary-Layer Parameters", NAVORD Report 4282, 1956
- (l) Schlichting, Hermann, "Boundary-Layer Theory", New York, McGraw Hill Book Co., 1955

Table I
Orifice Locations
(see also Figure 4)

Tap No.	BLUNT CONE			SHARP CONE	
	Angle of Elevation From Centerline (Degrees)	Azimuth Angle ψ (Degrees)	Distance Along Surface From Stagnation Point s (Inches)	Distance From Centerline (Inches)	s (Inches)
0	0	0	0		
1	10	45	0.262		
2	-20	225	0.524		
3	30	90	0.786		
4	-40	270	1.047		
5	50	135	1.309		
6	-60	315	1.571		
7	70	180	1.833		
8	-80	0	2.095		
<hr/>					
	Distance From Centerline Y (Inches)				
9	1.497	135	2.227		
10	1.522	90	2.359		
11	1.570	270	2.623		
12	1.629	315	2.940		
13	1.682	45	3.258		
14	2.740	90	9.365	2.740	15.776
15	2.740	225	9.365	2.740	15.776
16	2.740	315	9.365	2.740	15.776
Flat Base			10.865		17.276
17	On Sting at Intersection with Flat Base				
18	On Sting at Intersection with Spherical Base; 1.0625 inches downstream of Flat Base				

Table I (Cont)

BLUNT CONE	
Tap No.	Distance From Sting Along Base Surface (Inches)
19	0.830
20	1.140
21	1.460
22	1.770
23	2.080
24	2.400

APPENDIX A

CALCULATION OF THE BOUNDARY-LAYER DEVELOPMENT
ALONG THE CONE SURFACES

Laminar Flow

The region of laminar flow on a given body contour was calculated using a modified form of the compressible boundary-layer analysis for axially symmetrical flow given in reference (h). Inasmuch as the transitional and turbulent flow regions were computed by a stepwise solution of the boundary-layer momentum equation

$$\frac{d\theta}{ds} = \frac{C_f}{2} - \theta \left[\frac{((\delta^*/\theta)+2)}{U_e} \frac{dU_e}{ds} + \frac{1}{\rho_e} \frac{d\rho_e}{ds} + \frac{1}{Y} \frac{dY}{ds} \right] \quad (1A)$$

it was necessary to revise the analysis of reference (h) so that equation (1A) (which is applicable for laminar, transitional and turbulent flows) could be used over the entire body.

The following analysis is partially presented also in reference (i).

To start the calculations, it was stipulated that

$$\left. \frac{d\theta}{ds} \right|_{s=0} = 0 \quad (2A)$$

so

$$\left(\frac{C_f}{2} \right)_{Lam.} = \theta \left[\frac{(\delta^*/\theta)_{Lam} + 2}{U_e} \frac{dU_e}{ds} + \frac{1}{\rho_e} \frac{d\rho_e}{ds} + \frac{1}{Y} \frac{dY}{ds} \right] \quad (3A)$$

At a point on the surface of the model very close to the stagnation point, the values of U_e , ρ_e , and Y and their derivatives and the temperatures T_o and T_e were evaluated from the model geometry and the experimentally determined pressure distribution. A trial value of θ was assumed and the following relations from reference (h) as revised in reference (i) were solved by an iterative procedure until equation (3A) was balanced.

$$\frac{C_{fLam}}{2} = \frac{\ell}{Re_\theta} \left(\frac{T_o}{T_{ad}} \right)^{1/4} \quad (4A)$$

$$\text{and } \left(\frac{\delta^*}{\theta} \right)_{Lam} = H_{inc} \left(\frac{T_o}{T_e} \right) + \frac{T_o}{T_e} - 1 \quad (5A)$$

where

$$\ell = an^b + 0.22 \quad (6A)$$

$$H_{inc} = cn^d + e \quad (7A)$$

The equations for ℓ and H_{inc} were obtained by empirically fitting the correlation curves shown in reference (h) as Figures 1 and 6, respectively, for only the favorable pressure gradient regions.

The empirical constants a, b, c, d, and e were computed using the following expressions (reference i):

$$a = -1.106(S_w)^{0.924} + 1.28 \quad (8A)$$

$$b = -0.088(S_w)^{4.533} + 0.903 \quad (9A)$$

$$c = 7.776 S_w^3 + 16.125 S_w^2 + 7.151 S_w - 2.363 \quad (10A)$$

$$d = 0.328 S_w^3 + 0.034 S_w^2 - 0.174 S_w + 0.73 \quad (11A)$$

$$e = 2.6 (S_w + 1) \quad (12A)$$

$$S_w = \frac{T_w}{T_o} - 1 \quad (13A)$$

finally

$$n = \frac{\theta^2}{v_e} \frac{dU_e}{ds} \frac{T_o}{T_e} \text{ from reference (i)} \quad (14A)$$

For the sharp cone, with no heat transfer and zero pressure gradient, equation (1A) reduces to

$$\frac{d\theta}{ds} = \frac{\text{constant}}{\theta} = \frac{\theta}{s} \quad (15A)$$

$$\text{where, constant} = \frac{\ell \mu_e}{\rho_e U_e} \left(\frac{T_e}{T_{ad}} \right)^{1/4} \quad (16A)$$

$$\text{and } \ell = 0.22 \quad (17A)$$

Transition Region Flow

The start of boundary-layer transition was determined by a semi-empirical method. This method necessitated the knowledge of the location of the end of transition which coincided with the beginning of the fully turbulent boundary layer. Schlieren pictures taken for all test conditions furnished this information. The transition region calculations were started at some point and continued until the local skin friction

NAVORD Report 5668

coefficient $C_{f_{TR}} = C_{f_{Turb}}$ at the location determined from schlieren photographs. This means several trial calculations had to be made to locate the start of transition, but for any one model and surface configuration, the momentum thickness Reynolds number of transition was constant for varying free-stream Reynolds numbers as can be seen from comparison of Figures 9 and 10 of the text.

The details of the following analysis, are given in reference (f).

At the specified transition location, the values $C_{f_{TR}}$ and $(\delta^*/\theta)_{TR}$ for use in the following equation

$$\frac{d\theta}{ds} = \frac{C_{f_{TR}}}{2} - \theta \left[\frac{(\delta^*/\theta)_{TR} + 2}{U_e} \frac{dU_e}{ds} + \frac{1}{\rho_e} \frac{d\rho_e}{ds} + \frac{1}{Y} \frac{dY}{ds} \right] \quad (18A)$$

are to be computed as follows. Using the equation

$$C_{f_{TR}} = C_{f_{Turb}} - \frac{\text{constant}}{Re_\theta^2} \quad (\text{reference i}) \quad (19A)$$

where $C_{f_{Turb}}$ is calculated using the procedure described in reference (j). The constant is calculated at the start of transition where $C_{f_{TR}} = C_{f_{Lam}}$. Re_θ is known from the laminar calculations. Once the constant has been determined subsequent values of $C_{f_{TR}}$ are computed from equation (19A). At the observed location of the end of transition as determined from schlieren photographs

$$C_{f_{TR}} = C_{f_{Turb}} \quad (20A)$$

Figures A1 and A2 are plots of the experimentally determined location of the end of transition.

To compute $(\delta^*/\theta)_{TR}$ use

$$\left(\frac{\delta^*}{\theta}\right)_{TR} = \frac{\int_0^\delta \left(1 - \frac{T_e U}{T U_e}\right) c \left(\frac{Y}{\delta}\right)}{\int_0^\delta \frac{T_e U}{T U_e} \left(1 - \frac{U}{U_e}\right) d \left(\frac{Y}{\delta}\right)} \quad (21A)$$

where

$$\frac{U}{U_e} = \left(\frac{Y}{\delta}\right)^{\frac{1}{n_{TR}}} \quad (22A)$$

$$\text{and } \frac{T}{T_e} = \frac{T_{ad}}{T_e} - \frac{T_{ad} - T_e}{T_e} \left(\frac{U}{U_e}\right)^2 \quad (23A)$$

for zero heat transfer

$$\text{and } n_{TR} = 1.25 + 5.25 \times 10^{-3} \Delta Re_{\theta} - 1.9 \times 10^{-6} (\Delta Re_{\theta})^2 \quad (24A)$$

where

$$\Delta Re_{\theta} = Re_{\theta} - Re_{\theta,TR, \text{ start}} \quad (25A)$$

Equation (18A) reduces to

$$\frac{d\theta}{ds} = \frac{C_{f,TR}}{2} = \frac{\theta}{s} \text{ for the sharp cone} \quad (26A)$$

Figure A3 is a plot of the skin friction coefficient showing the transition from laminar to turbulent boundary layer.

Turbulent Flow

The details of the following analysis are given in reference (j)

At the position along the surface where a fully turbulent flow is assumed to exist the following relations are used to calculate $C_{f,Turb}$ and $(\delta^*/\theta)_{Turb}$ for use in the following equation

$$\frac{d\theta}{ds} = \frac{C_{f,Turb}}{2} = \theta \left[\frac{(\delta^*/\theta)_{Turb} + 2}{U_e} \frac{dU_e}{ds} + \frac{1}{\rho_e} \frac{d\rho_e}{ds} + \frac{1}{Y} \frac{dY}{ds} \right] \quad (27A)$$

From reference (j)

$$\frac{C_{f,Turb}}{2} = (20\bar{n})^{\frac{1-\bar{n}}{1+\bar{n}}} \left(\frac{\theta/\delta}{Re_{\theta}}\right)^{\frac{2}{\bar{n}+1}} \left(\frac{T_e}{T_L}\right)^{\frac{\bar{n}-2\omega-1}{\bar{n}+1}} \quad (28A)$$

$$\frac{U_L}{U_e} = \left(\frac{20\bar{n}(\theta/\delta)}{Re_{\theta}}\right)^{\frac{1}{\bar{n}+1}} \left(\frac{T_L}{T_e}\right)^{\frac{\omega+1}{\bar{n}+1}} \quad (29A)$$

$$\frac{T_L}{T_e} = \frac{T_{ad}}{T_e} - \frac{T_{ad} - T_e}{T_e} \left(\frac{U_L}{U_e}\right)^2 \quad (30A)$$

where the subscript L refers to values at the edge of the laminar sublayer

and

$$\delta^*/\theta_{Turb} = \frac{\int_0^{1.0} \left(1 - \frac{T_e U}{T U_e}\right) d\left(\frac{Y}{\delta}\right)}{\int_0^{1.0} \frac{T_e U}{T U_e} \left(1 - \frac{U}{U_e}\right) d\left(\frac{Y}{\delta}\right)} \quad (31A)$$

with $\frac{U}{U_e} = (Y/\delta)^{1/\bar{n}}$ (32A)

where $\bar{n}_{Turb} = 2.05 \log_{10} Re_{\theta} - 1.65$ (33A)

and $\omega =$ Exponent in the viscosity temperature relationship

$$\omega = 0.76$$

$$\frac{T}{T_e} = \frac{T_{ad}}{T_e} - \frac{T_{ad} - T_e}{T_e} \left(\frac{U}{U_e}\right)^2 \quad (34A)$$

Values of $\frac{\theta}{\delta}$ for use in equations (28A) and (25A) are computed using

$$\frac{\theta}{\delta} = \int_0^{1.0} \frac{T_e U}{T U_e} \left(1 - \frac{U}{U_e}\right) d\left(\frac{Y}{\delta}\right) \quad (35A)$$

with equation (32A)

Values of $\frac{\theta}{\delta}$ and $(\delta^*/\theta)_{Turb}$ are tabulated for a wide range of Mach numbers and values of \bar{n} in reference (k).

Equation (27A) reduces to

$$\frac{d\theta}{ds} = \frac{C_{f_{Turb}}}{2} - \frac{\theta}{s} \text{ for the sharp cone} \quad (36A)$$

where

$C_{f_{TR}}$ and $C_{f_{Turb}}$ are computed as above, in equations (19A) and

(28A).

Effect of Surface Roughness

It was assumed that the effect of roughness could be neglected as long as the boundary layer stayed laminar.

For the rough blunt cone, using some unpublished results of J. Persh, the turbulent local skin friction is defined as

$$C_{f_{TurbR}} = C_{f_{Turb}} + \frac{Re_{k_s} \times 10^{-4}}{Re_0^{0.268} \times 10^{0.678 \left(\frac{\pi+2}{\pi}\right)}} \quad (37A)$$

where

$$Re_{k_s} = \frac{\rho_e U_e k_s}{\mu_e} \quad (38A)$$

and the transition region local skin friction coefficient is defined by

$$C_{f_{TransR}} = C_{f_{TurbR}} - \frac{\text{constant}}{Re_0^2} \quad (39A)$$

where k_s - the equivalent sand roughness, and the constant is again evaluated at the transition point, where

$$C_{f_{TransR}} = C_{f_{Lam}} \quad (40A)$$

The equivalent sand roughness was determined from Figure A4 which is a plot of experimental data taken from Figure 20:22 of reference (1). As the number 24 grain applied to the model is roughly conical in shape, the curve for cones in Figure A4 was considered most nearly applicable for the calculations. The average height of the roughness particles was determined from schlieren photographs and the ratio of the particle spacing to particle base size was taken as $d/D = 1$. The 1 to 1 ratio was used since it approximates that of the No. 24 grain on the model surface. The average elevation as taken

from schlieren photographs is $k = 0.0097$ inch, and $\frac{k_s}{k} = 2.6$ from Figure (A4) at $\frac{d}{D}$ of 1 therefore, $k_s = 0.02519$ inch. Using equations (21A), (37A), (38A), (39A), and (40A) the following equations were solved to determine the boundary-layer growth

NAVORD Report 5668

for the transitional and turbulent regions, respectively:

$$\frac{d\theta}{ds} = \frac{C_{f_{TRR}}}{2} - \theta \left[\frac{(\delta^*/\theta)_{TRR} + 2}{U_e} \frac{dU_e}{ds} + \frac{1}{\rho_e} \frac{d\rho_e}{ds} + \frac{1}{Y} \frac{dY}{ds} \right] \quad (41A)$$

and

$$\frac{d\theta}{ds} = \frac{C_{f_{TurbR}}}{2} - \theta \left[\frac{(\delta^*/\theta)_{Turb} + 2}{U_e} \frac{dU_e}{ds} + \frac{1}{\rho_e} \frac{d\rho_e}{ds} + \frac{1}{Y} \frac{dY}{ds} \right] \quad (42A)$$

Figures A5 and A6 are sample plots of the Reynolds number based on momentum thickness as determined from the above calculations over the sharp cone and blunt cone, respectively, while Figure 7 in the text is a plot of all the calculated Reynolds numbers based on momentum thickness at the end of the cone as a function of free-stream Reynolds number, in comparison with the momentum thickness Reynolds number obtained from the boundary-layer surveys.

APPENDIX B

EFFECTS OF SURFACE ROUGHNESS

The base pressure and wake flow investigations on both the sharp cone and the blunt cone were carried out in as large a common region of momentum thickness Reynolds numbers as possible in order to have sufficient comparative data in the laminar and turbulent boundary layer regime. For the sharp cone tests at Mach numbers of 2.66, 2.74, and 2.76 the supply pressure in the wind tunnel was varied from about 0.4 atmosphere to 1.6 atmospheres. This variation permitted a modification of boundary-layer development from completely laminar to turbulent over the downstream half of the cone. However, the blunt cone with the 125 micro-inch finish tested at $Ma_{\infty} = 4.84$ with an available maximum supply pressure of 3.5 atmospheres experienced only a laminar boundary layer. Consequently, it was necessary to produce transition on the body by boundary-layer tripping.

Attempts were made to trip the boundary layer with rings located downstream of the favorable pressure gradient region of the spherical nose of the blunt cone (see Figure 4 of the report). Ring elevations from 0.005 inch to 0.035 inch above the model surface were tested at $Ma_{\infty} = 4.74$ and supply pressures from 1 to 3.5 atmospheres. All trip ring elevations larger than 0.005 inch caused local shocks which were undesirable in view of the requirement that the surface pressure distribution should not be affected by roughness elements. Furthermore, as evidenced from spark schlieren photographs, all trip rings with the exception of the one with the largest elevation were ineffective with respect to boundary-layer tripping on the body surface. The largest trip ring (0.035 inch elevation) promoted only turbulence bursts near the end of the cone at the highest supply pressure.

Base pressures measured with the smallest and the largest trip ring applied are plotted as base to cone pressure ratio, p_b/p_c , versus free-stream Reynolds number in Figure B1 in comparison with the 125 micro-inch finish data, the data with distributed roughness (No. 24 grains) on the entire surface, and the sharp cone data (15 and 125 micro-inch finish). At the same free-stream Reynolds numbers the base pressure ratio was not affected at all by the 0.005 inch trip ring. This result was evident from the spark schlieren photographs. The base pressures obtained by application of the 0.035 inch trip ring show a distinct departure from the data obtained with

NAVORD Report 5668

the 0.005 trip ring. The larger negative slope of the base pressure data with increasing free-stream Reynolds number for the 0.035 trip ring indicates that the data extend into a region of larger momentum thickness Reynolds numbers, $Re_{\theta,c}$.

This is also evidenced by the appearance of turbulence bursts in the boundary-layer near the end of the cone. A quantitative correlation with $Re_{\theta,c}$ was not made since boundary-layer

surveys were not taken in connection with the trip ring tests and the inadequate performance of these single roughness elements did not justify local pressure distribution measurements and a modification of the calculation procedure for the boundary-layer development in order to obtain $Re_{\theta,c}$ data.

However, it appears plausible to assume that the base pressure data would fall in line with the base pressure ratio versus $Re_{\theta,c}$ curve given in Figure 11.

Application of the No. 24 grain carborundum powder lead to an effective average roughness element height of 0.0097 inch which did not affect the surface pressure distribution. Boundary-layer transition occurred at about five inches ahead of the base at a supply pressure of 3.5 atmospheres. The base pressures measured with this roughness reached the same absolute minimum as the sharp cone (Figure B1). The corresponding momentum thickness Reynolds numbers ($Re_{\theta,c} = 1630$) were the same.

Later tests at NOL on other models indicated that a smaller grain size roughness would have been sufficient to promote a turbulent boundary layer. It is conceivable that oversized roughness elements particularly in the thin boundary-layer region at the nose could lead to energy dissipation into the potential flow. Consequently, in severe cases laminar boundary-layer separation could occur. However, the undisturbed surface pressure distribution measured with the No. 24 grain distributed roughness indicated that the potential flow about the blunt cone was not adversely affected.

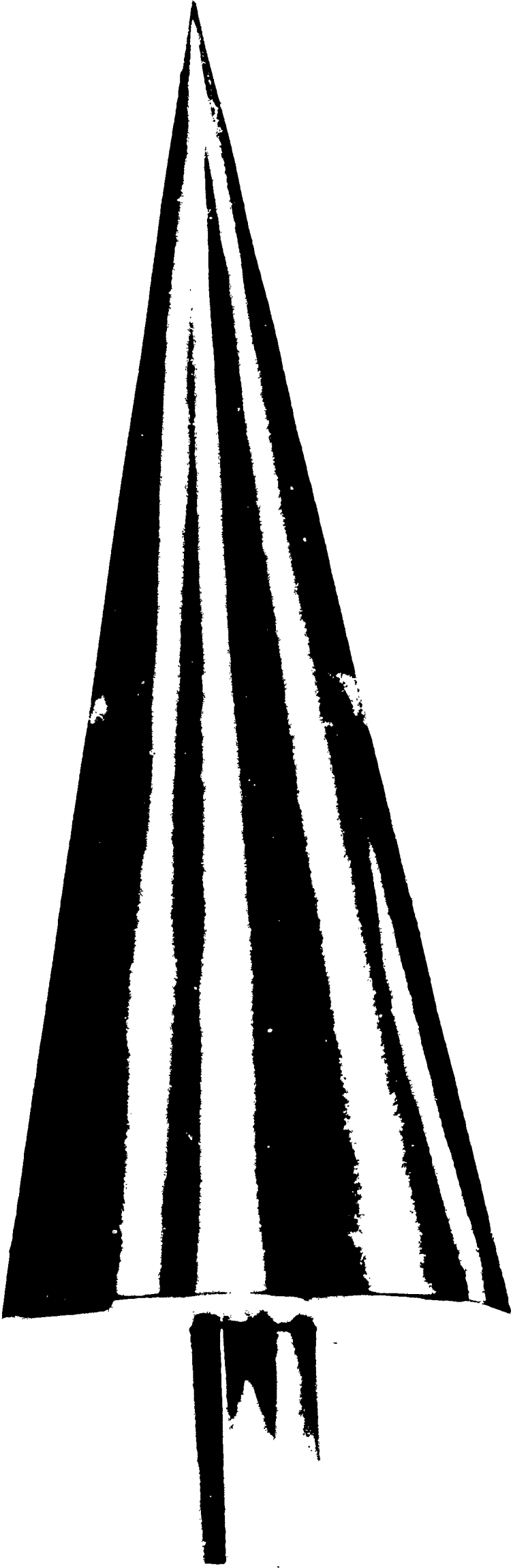


FIG. 1 10° SHARP CONE WITH MOUNTING STING



FIG 2 10° SPHERE CONE WITH MOUNTING STING



FIG. 3 10° SPHERE CONE WITH SPHERICAL BASE AND MOUNTING STING

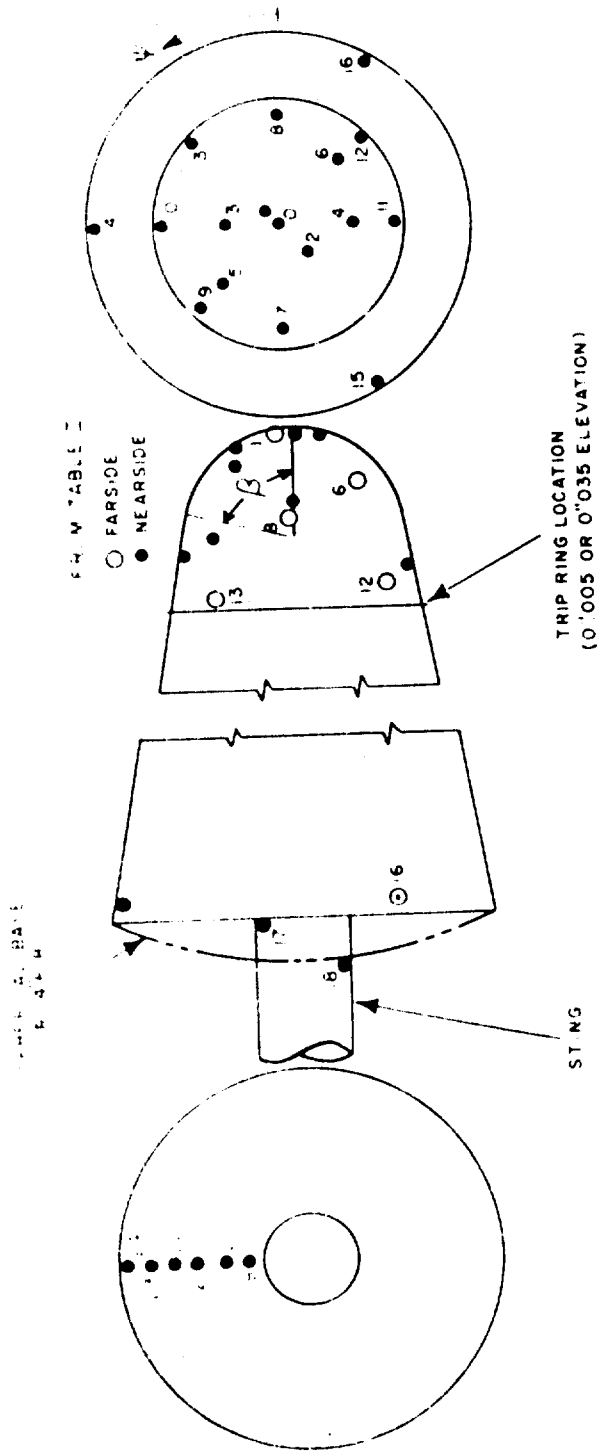


FIG 4 DIAGRAM OF ORIFICE LOCATIONS AND SINGLE ROUGHNESS ELEMENTS



FIG 5 10° SPHERE CONE WITH NO. 24 GRAIN DISTRIBUTED SURFACE ROUGHNESS
MOUNTED IN THE WIND TUNNEL TEST SECTION

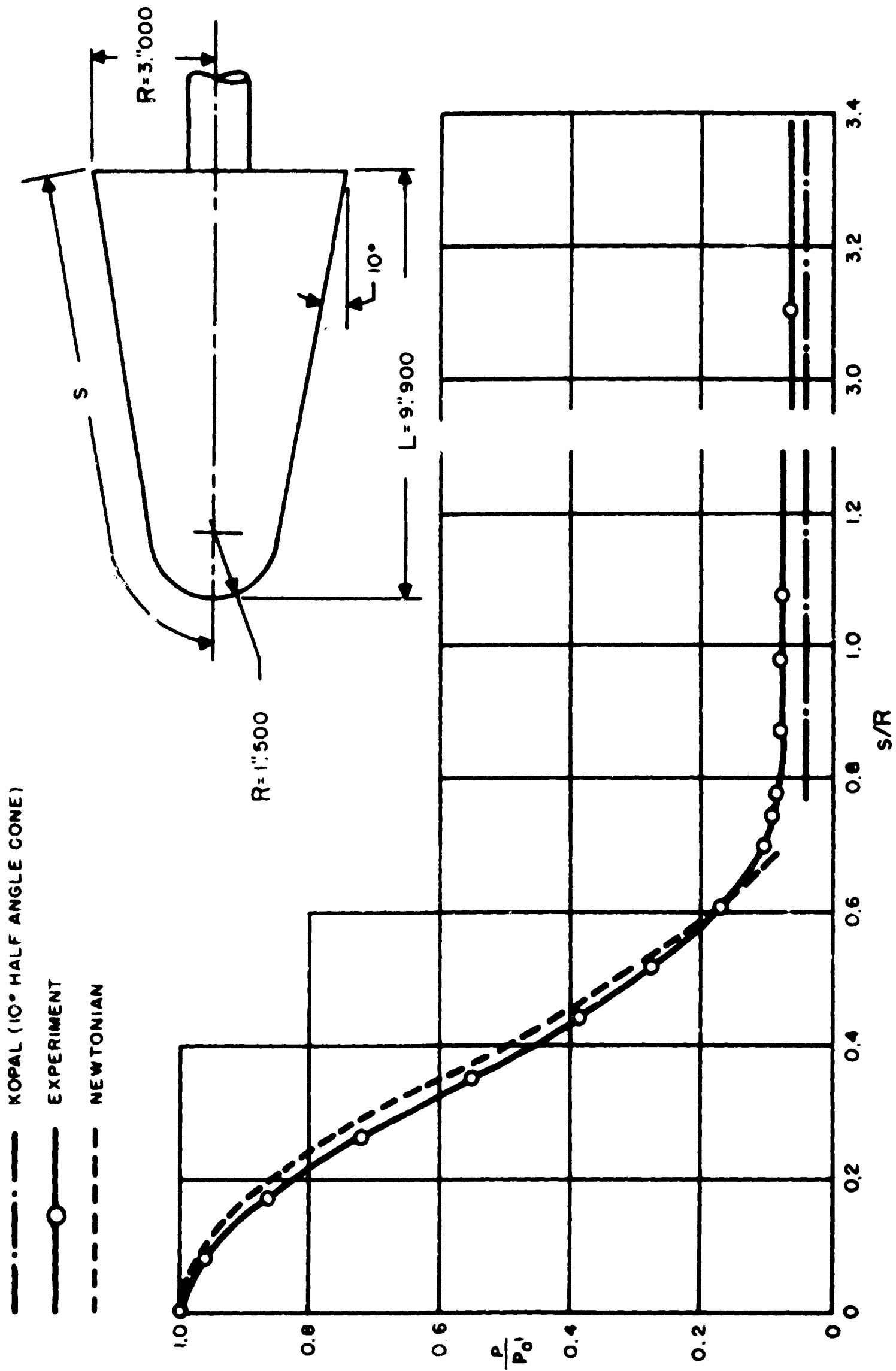
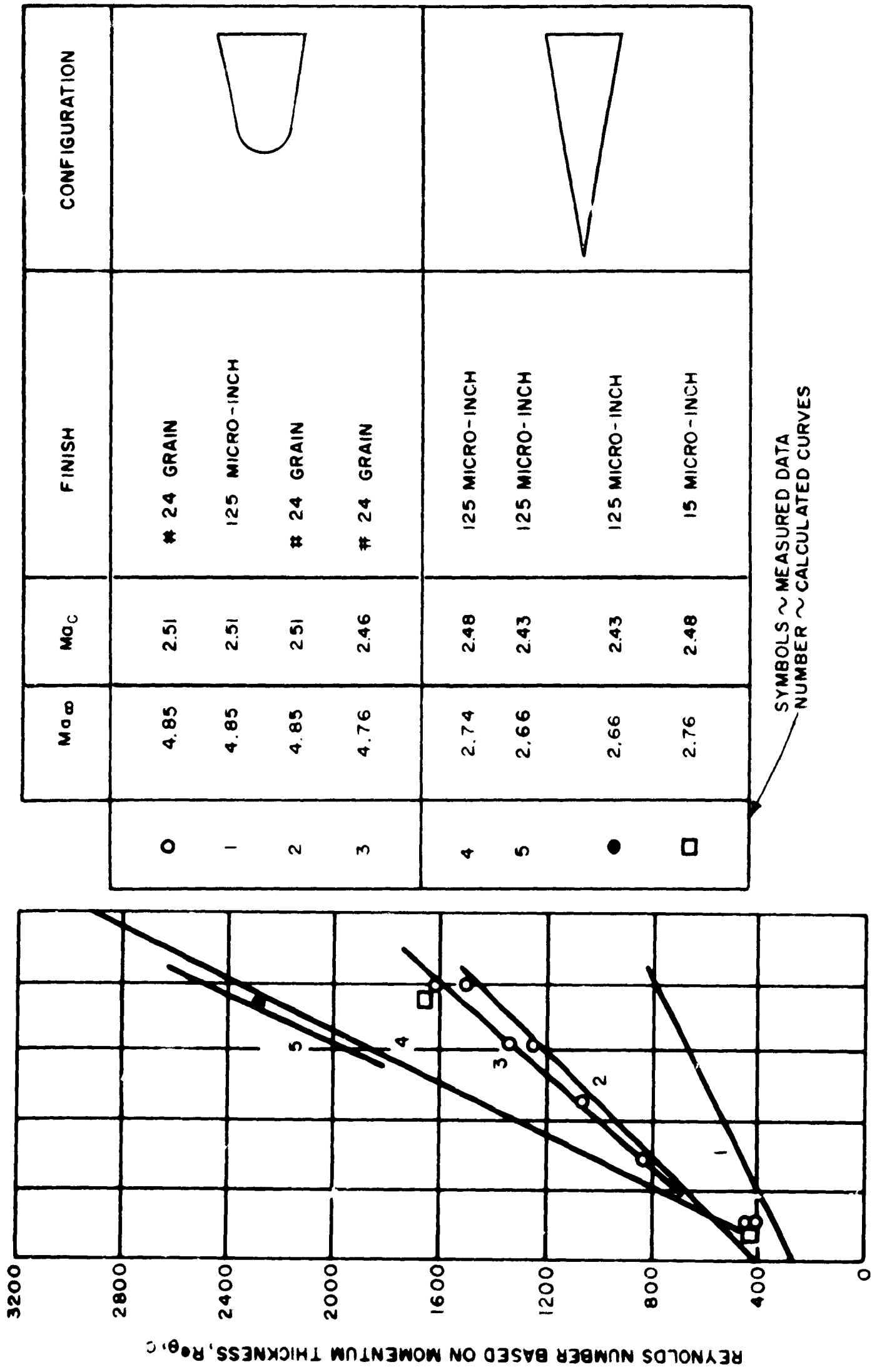


FIG. 6 SURFACE PRESSURE DISTRIBUTION ON THE 10° SPHERE CONE AT $M_\infty = 4.74$



SYMBOLS ~ MEASURED DATA
 NUMBER ~ CALCULATED CURVES

FREE STREAM REYNOLDS NUMBER PER FOOT, $Re_{\infty}/FT \times 10^{-6}$

FIG. 7 MOMENTUM THICKNESS REYNOLDS NUMBER AS A FUNCTION OF FREE STREAM REYNOLDS NUMBER PER FOOT



W. J. ...
 ...
 ...

W. J. ...
 ...
 ...

FIG. 8. SHARP CONE'S PHOTOGRAPHS OF THE 10° SHARP CONE

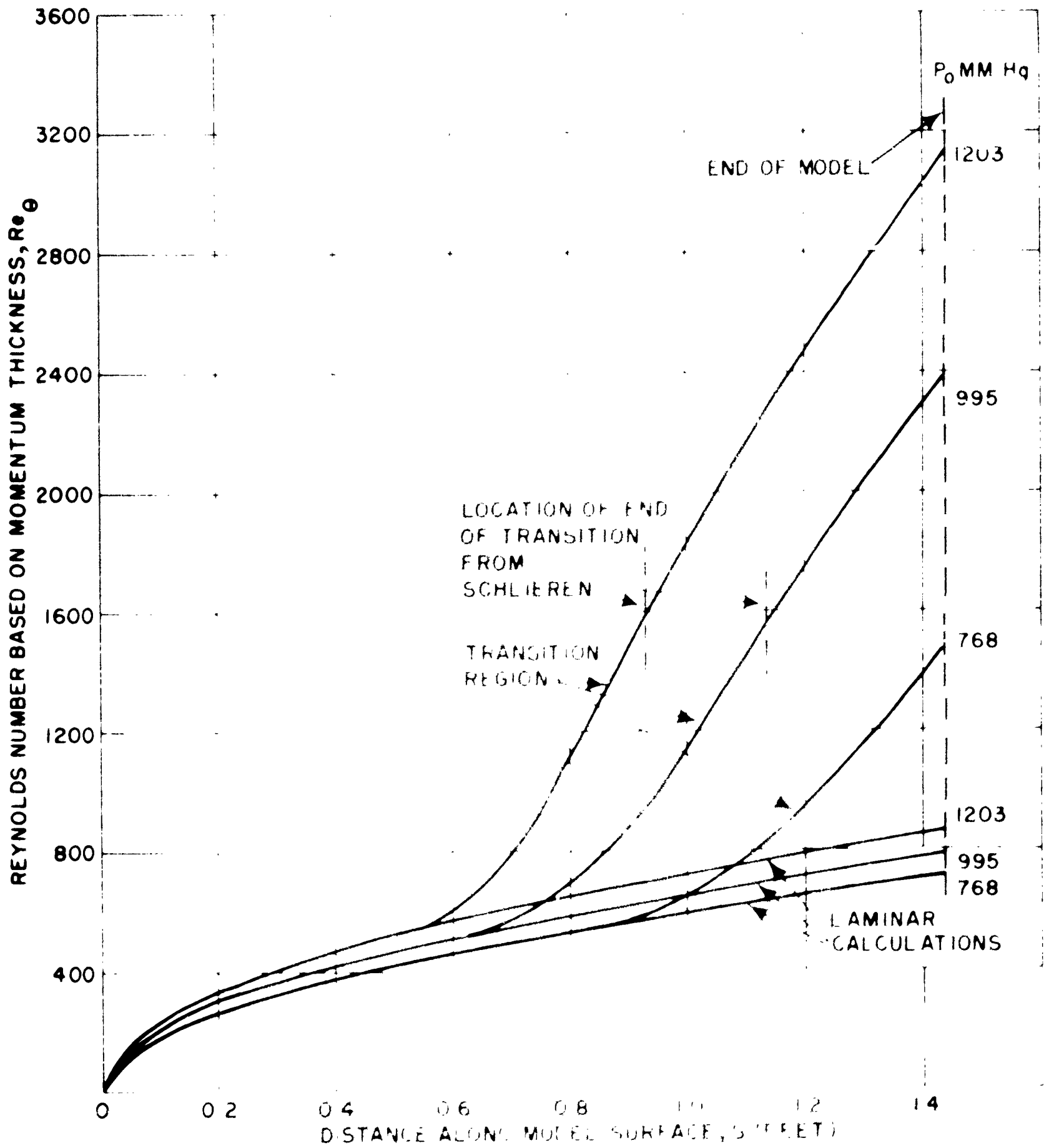


FIG. 9 MOMENTUM THICKNESS REYNOLDS NUMBER DISTRIBUTION ON 10° SHARP CONE, $Ma_\infty = 2.74$, 125 MICRO-INCH FINISH

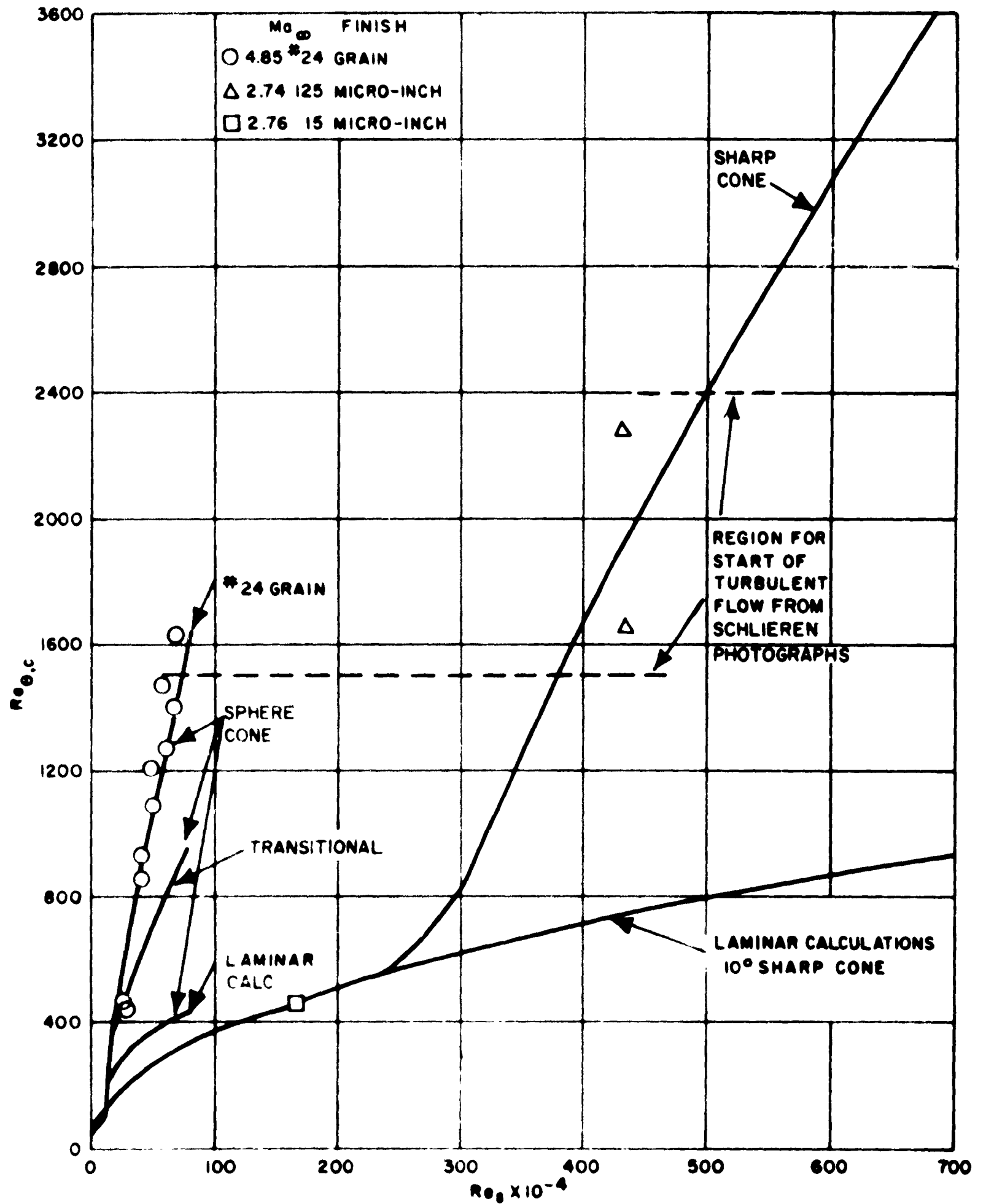


FIG. 10 MOMENTUM THICKNESS AS A FUNCTION OF DISTANCE ALONG MODEL SURFACE IN TERMS OF REYNOLDS NUMBER

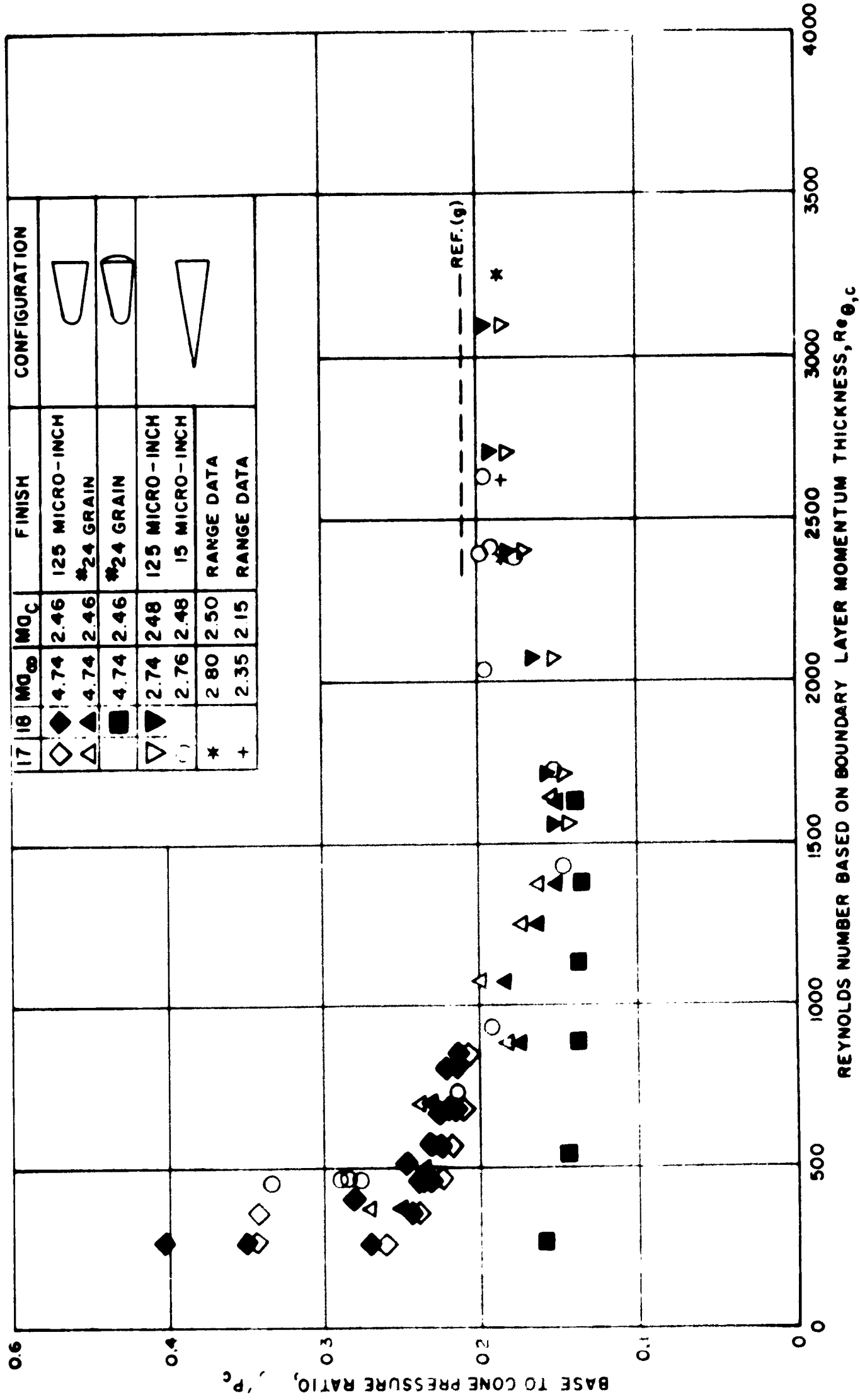
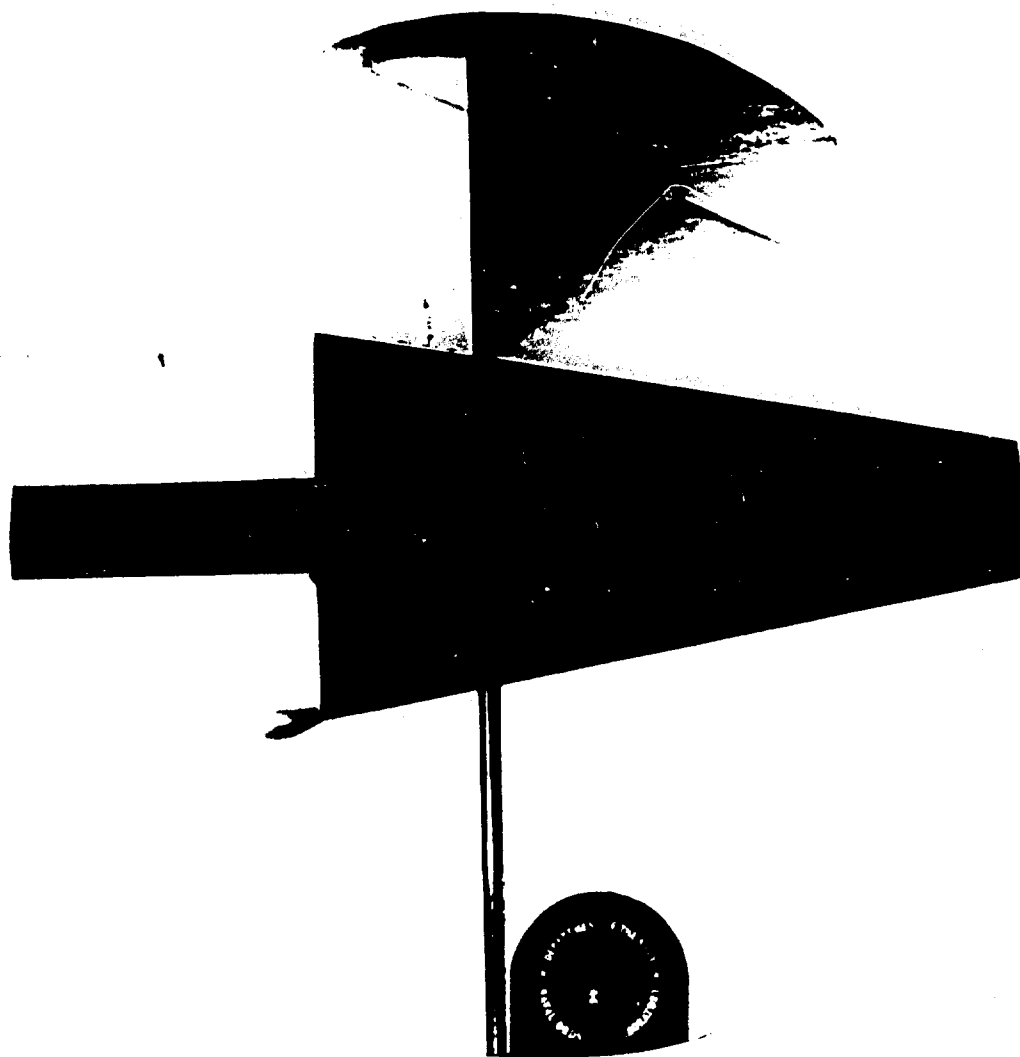


FIG. 11 BASE PRESSURE RATIO OF THE 10° SHARP CONE AND THE 10° SPHERE CONE AS A FUNCTION OF $Re_{\theta,c}$

NAVORD REPORT 5068



WAKE ANGLE

FIGURE 1. INTERFEREN PHOTOGRAPH (1/100 SEC) OF THE 10°
SHARP CONE AT $Ma_\infty = 2.70$ AND $Re_{\theta,c} = 2470$

NAVORD REPORT 5668

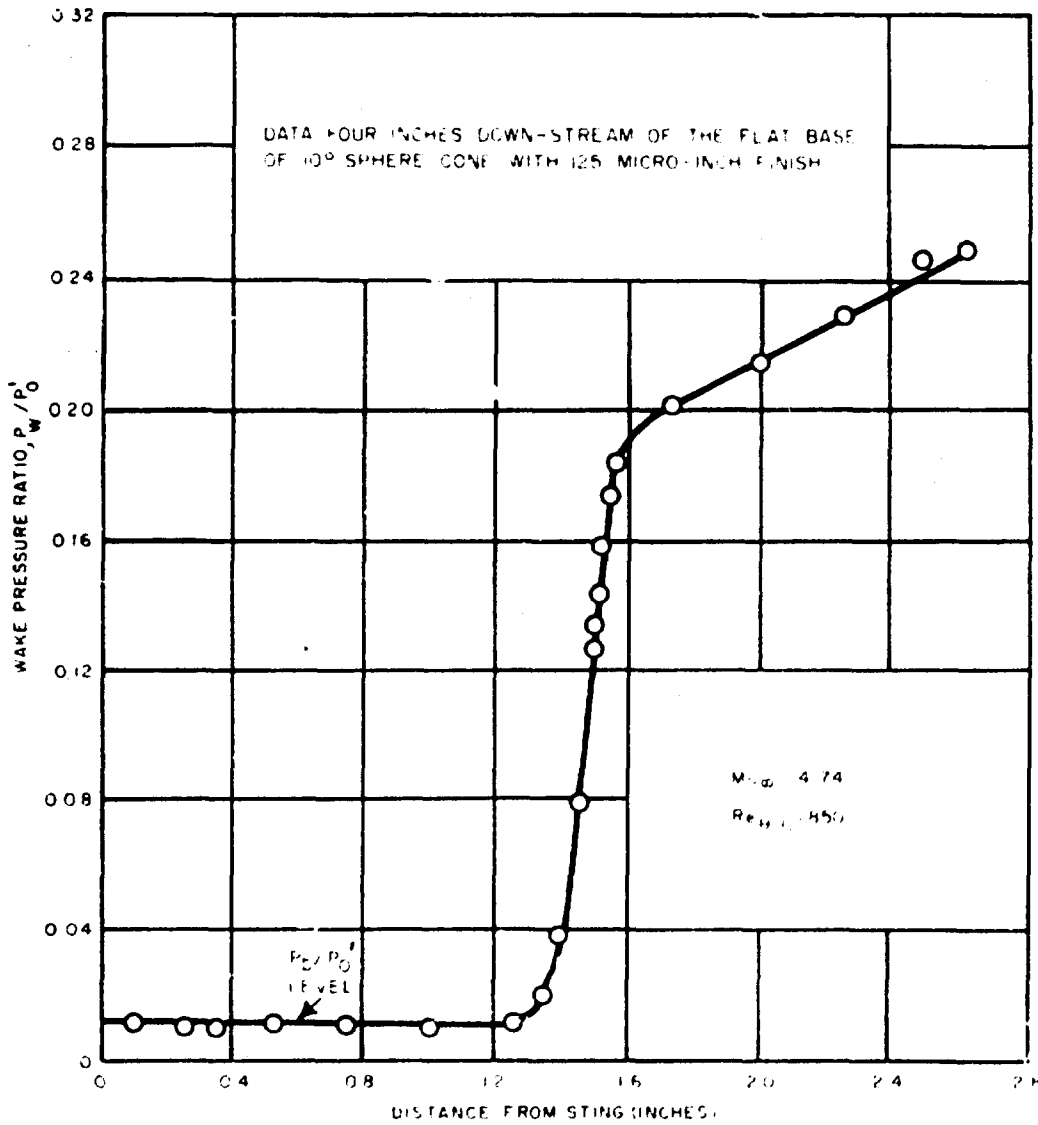


FIG. 13 TOTAL PRESSURE WAKE PROFILE FOR THE 10° SPHERE CONE

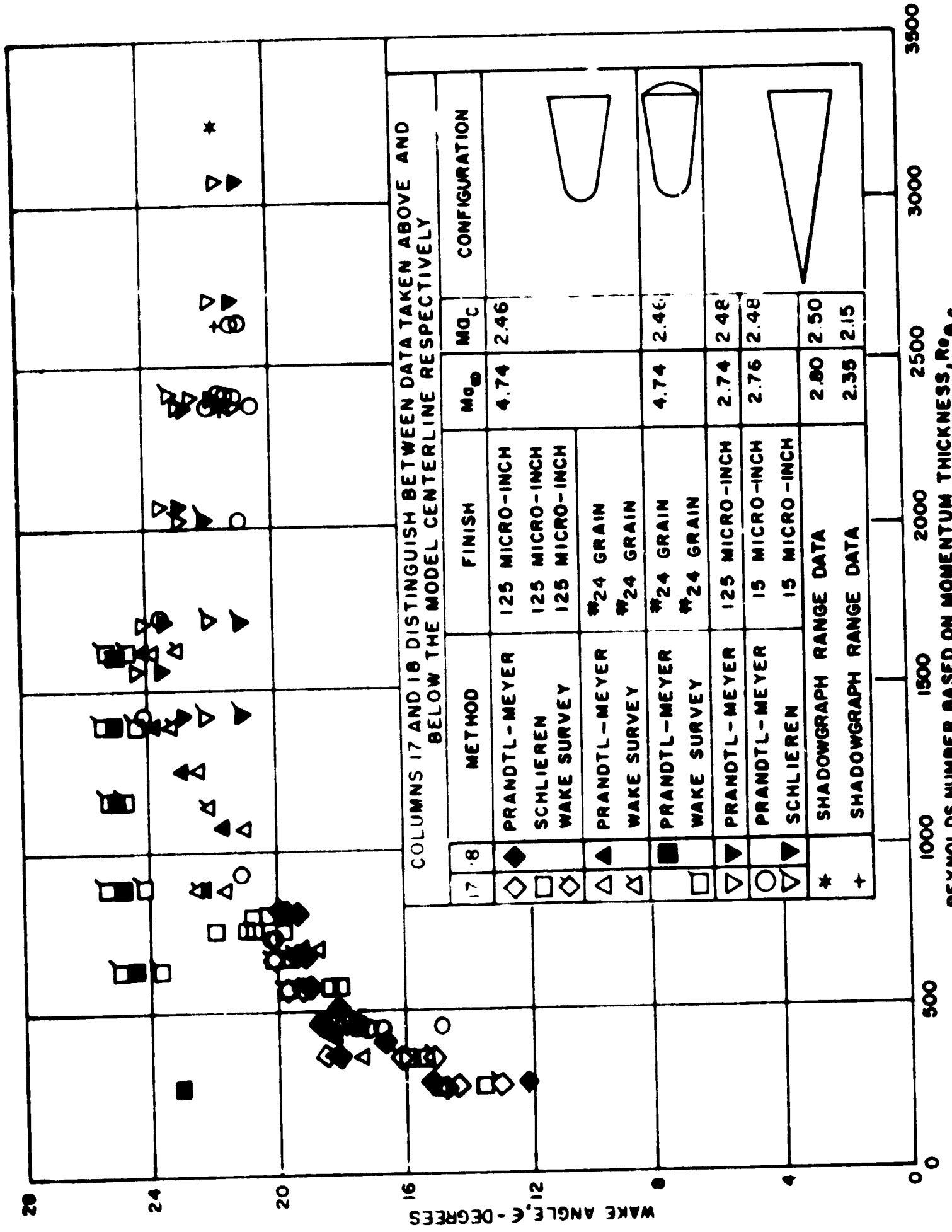


FIG. 14 WAKE ANGLE OF 10° SHARP CONE AND 10° SPHERE CONE AS A FUNCTION OF $Re_{\theta,c}$

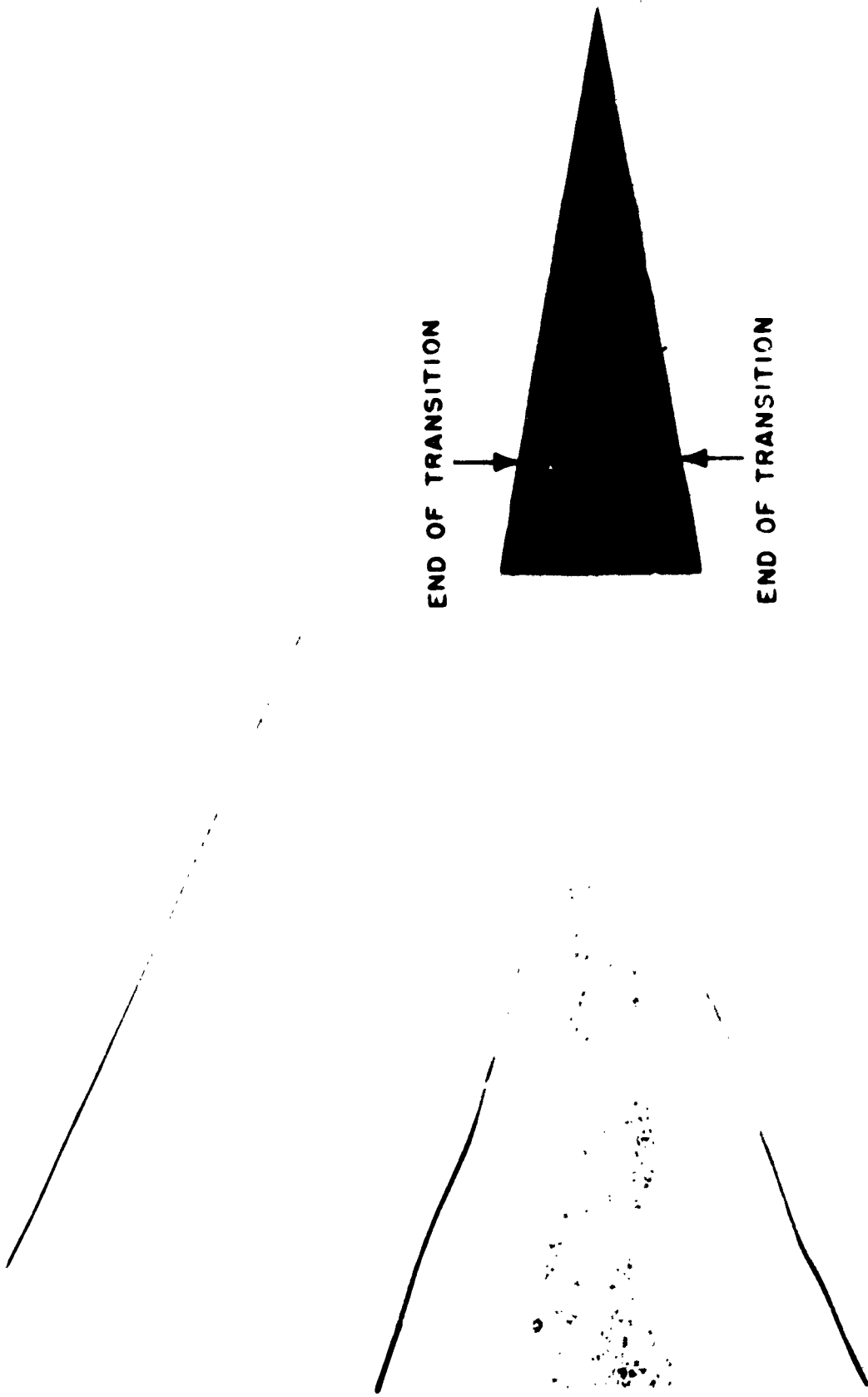


FIG. 15 SHADOWGRAPH OF A 10° SEMIVERTEX ANGLE CONE AT $M_{\infty} = 2.35$

NAVORD REPORT 5668

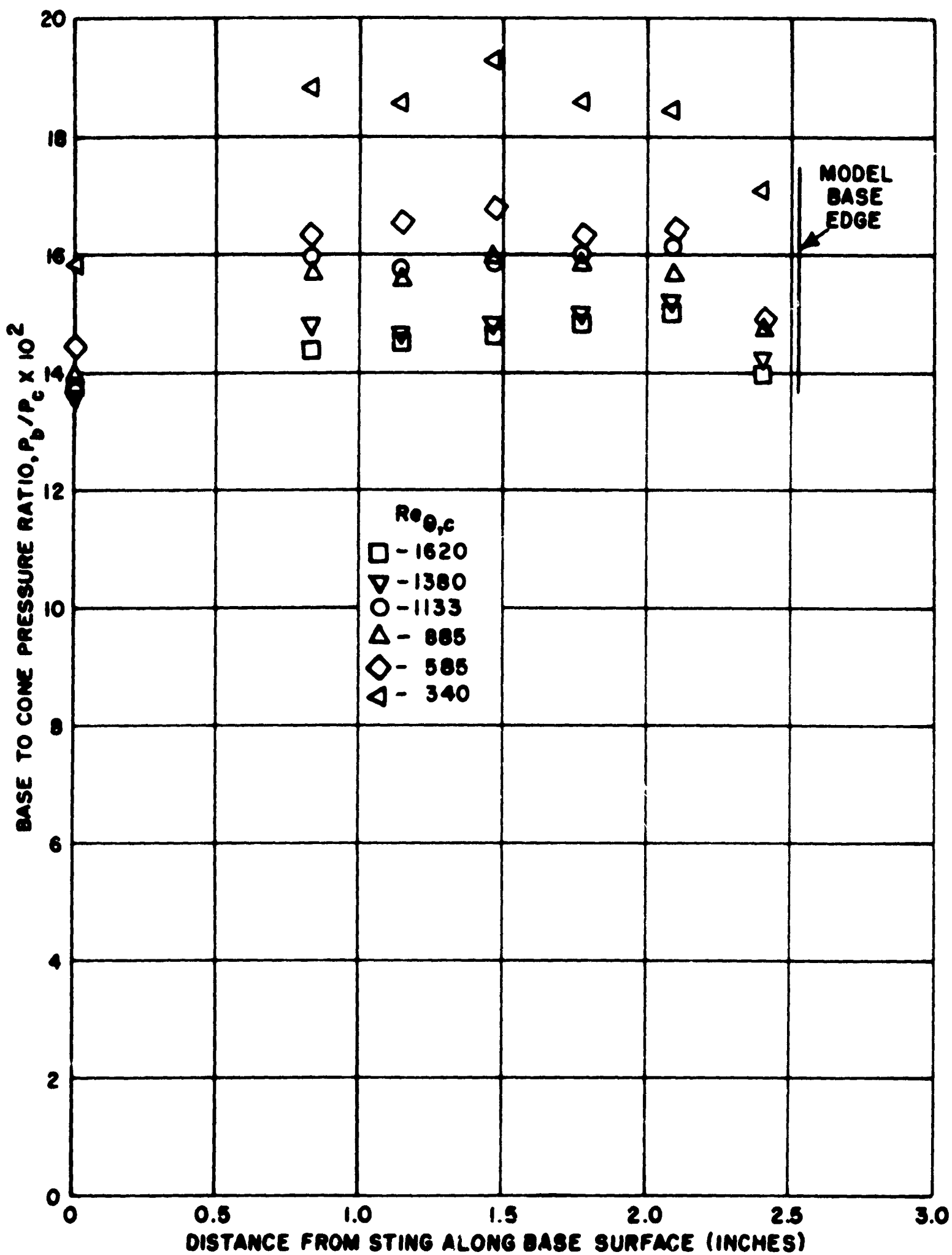


FIG. 16 BASE PRESSURE DISTRIBUTION ON THE
ROUGH 10° SPHERE CONE WITH SPHERICAL
BASE AT $M_\infty = 4.74$

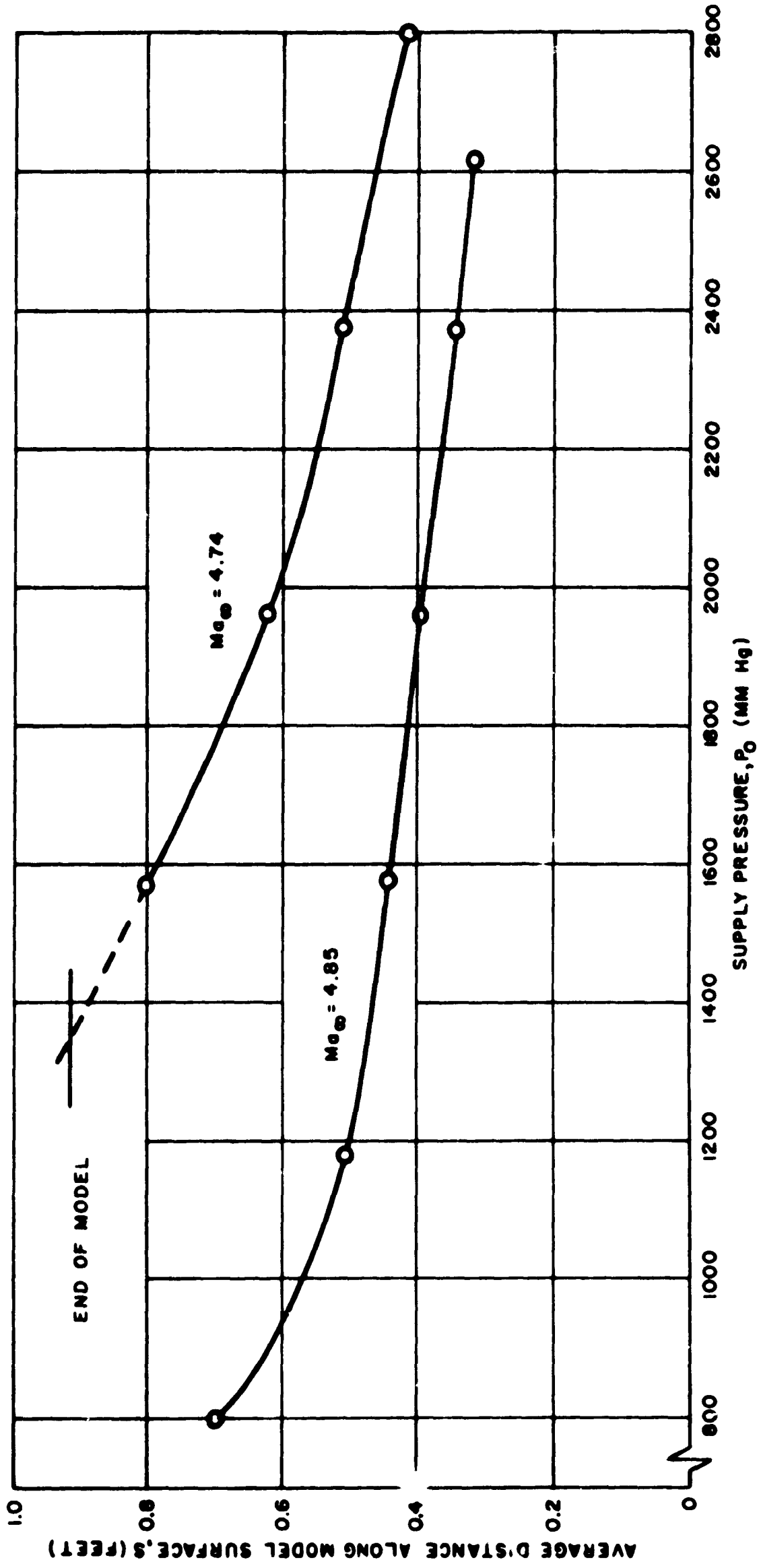


FIG. A1 LOCATION OF THE END OF TRANSITION AS A FUNCTION OF SUPPLY PRESSURE FOR THE ROUGH 10° SPHERE CONE

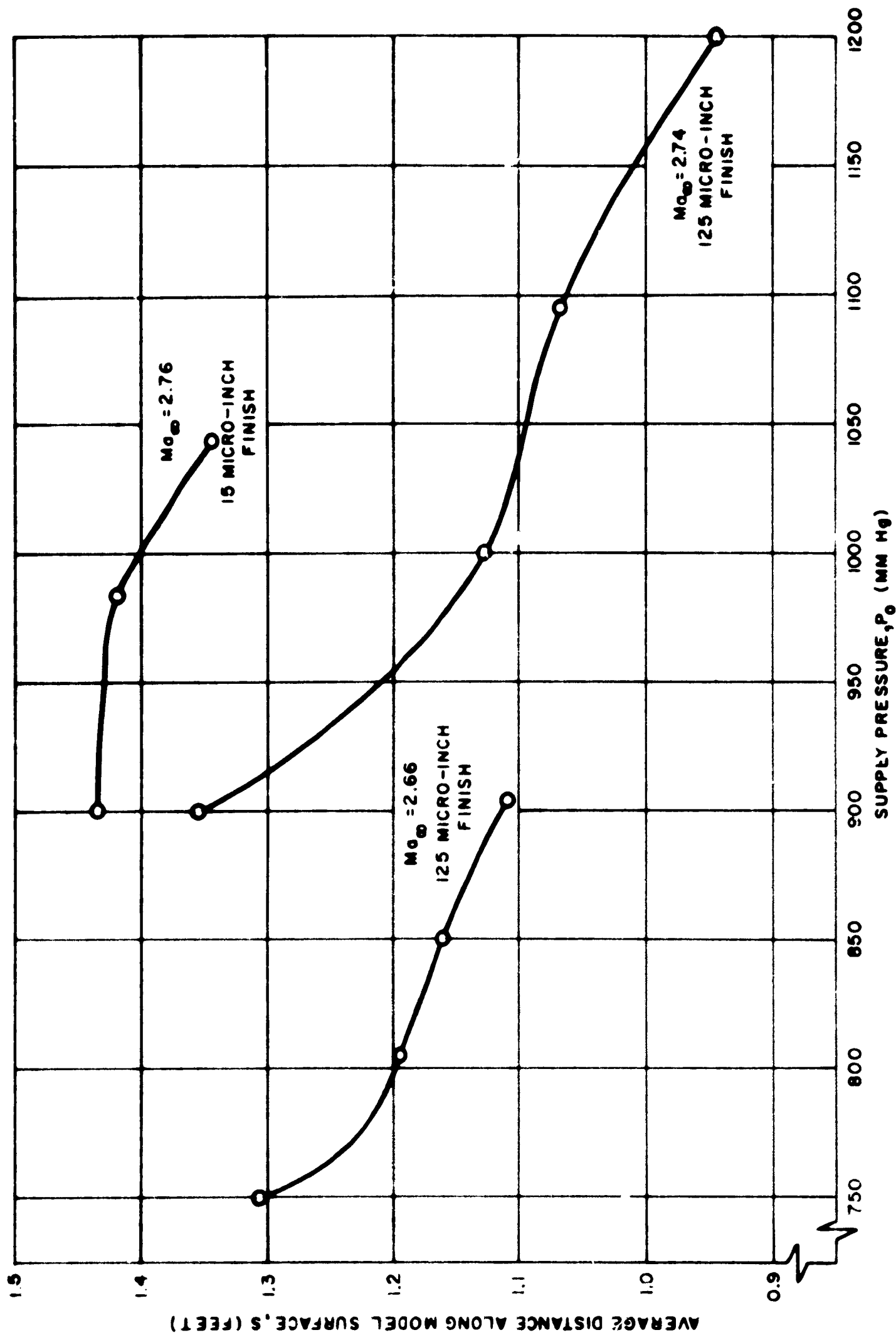


FIG. A2 LOCATION OF THE END OF TRANSITION AS A FUNCTION OF SUPPLY PRESSURE FOR THE 10° SHARP CONE

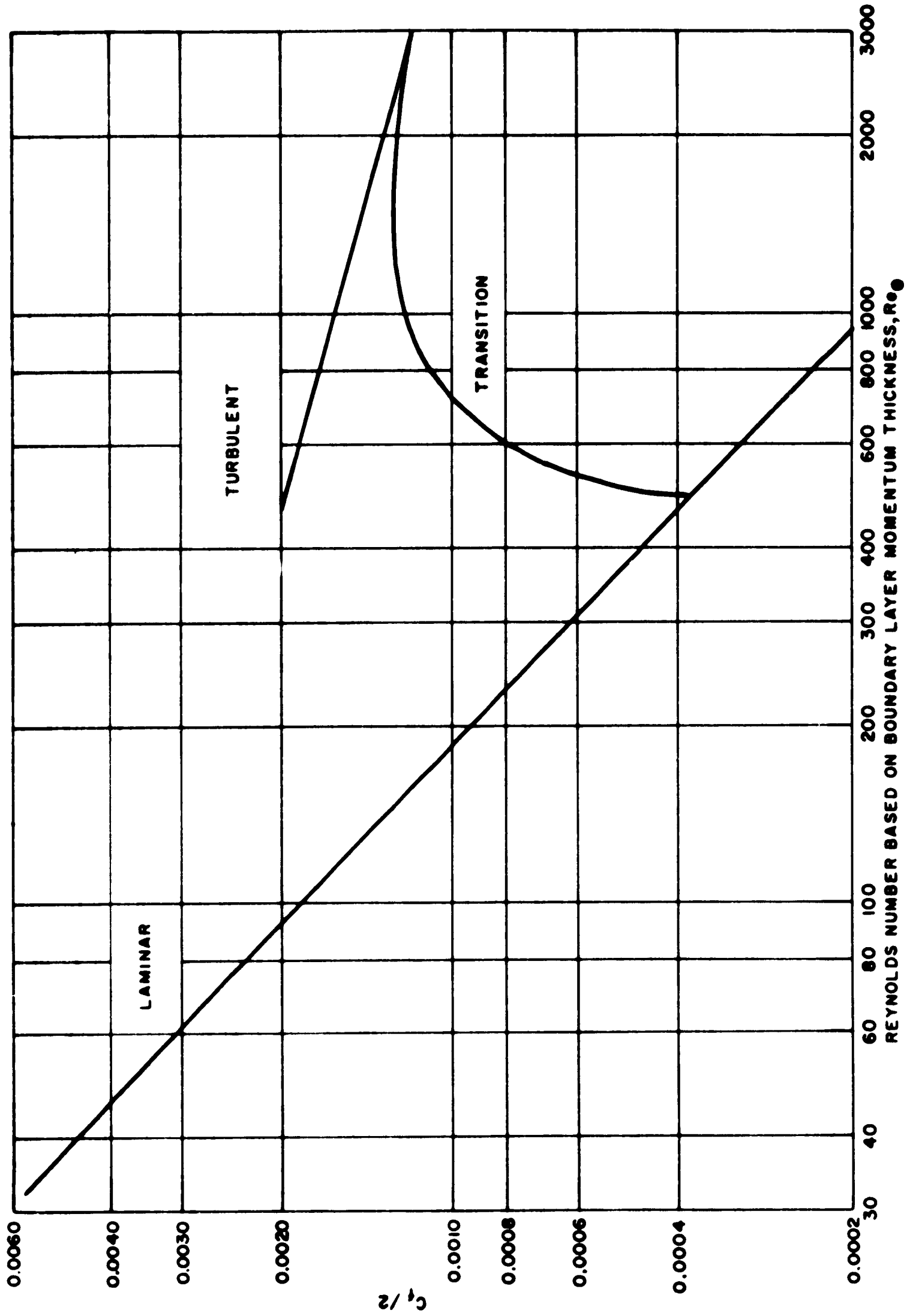


FIG. A3 LOCAL SKIN FRICTION COEFFICIENT AS A FUNCTION OF Re_θ FOR 10° SHARP CONE

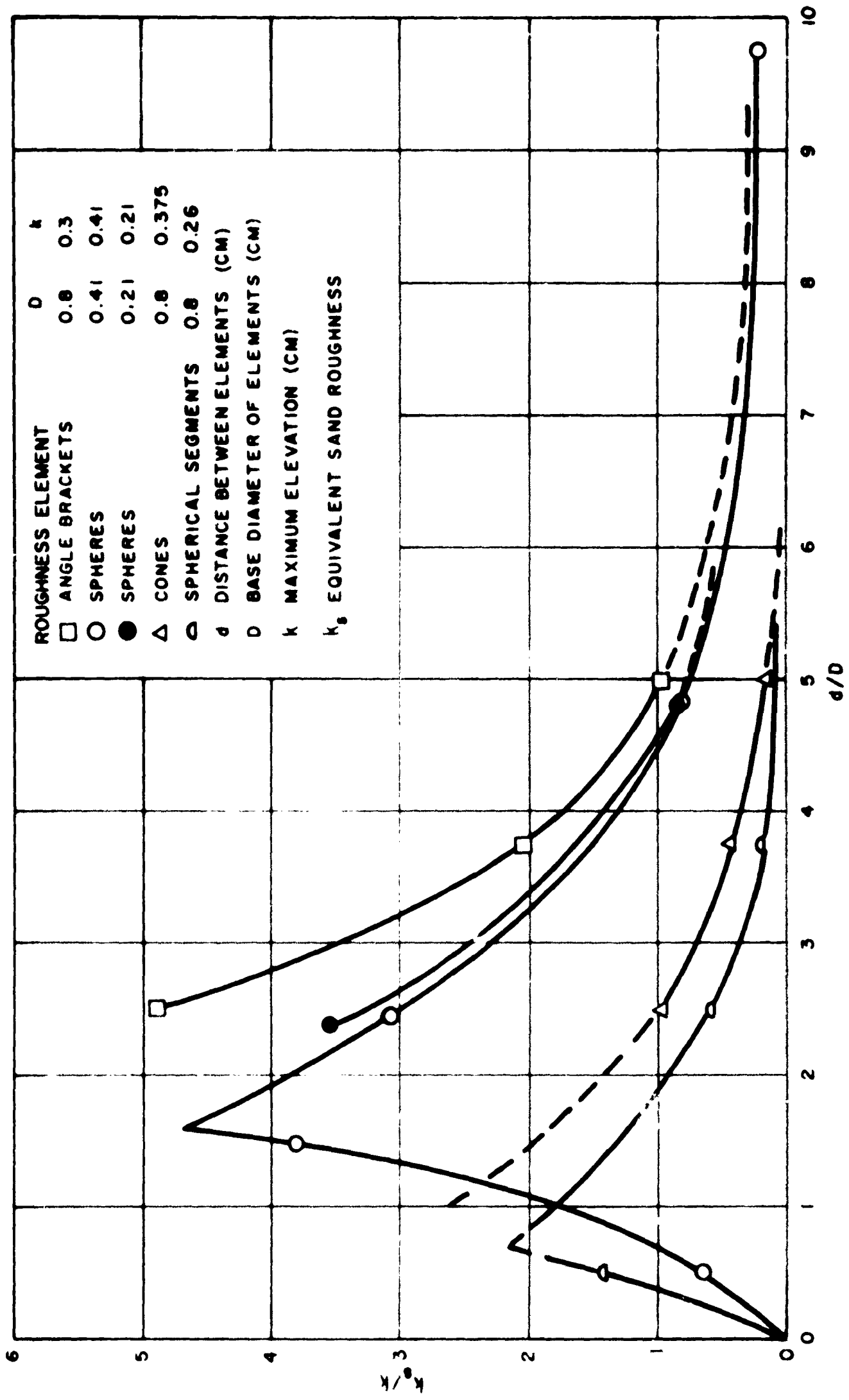


FIG. A4 RESULTS OF MEASUREMENTS ON REGULAR ROUGHNESS PATTERNS (REF.1)

NAVORD REPORT 5668

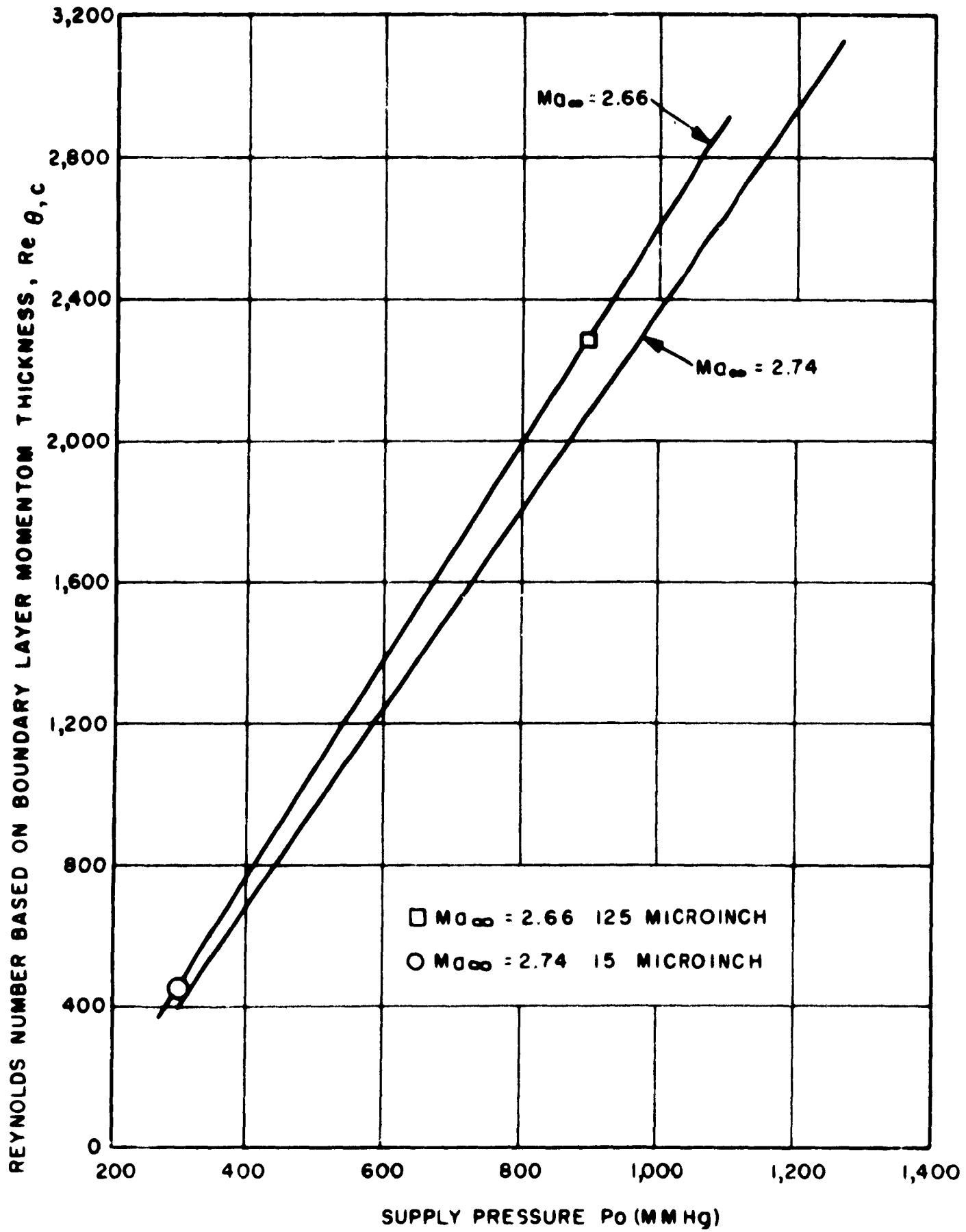


FIG. A5 REYNOLDS NUMBER, $Re_{\theta,c}$, AS A FUNCTION OF SUPPLY PRESSURE, P_0 , FOR THE 10° SHARP CONE

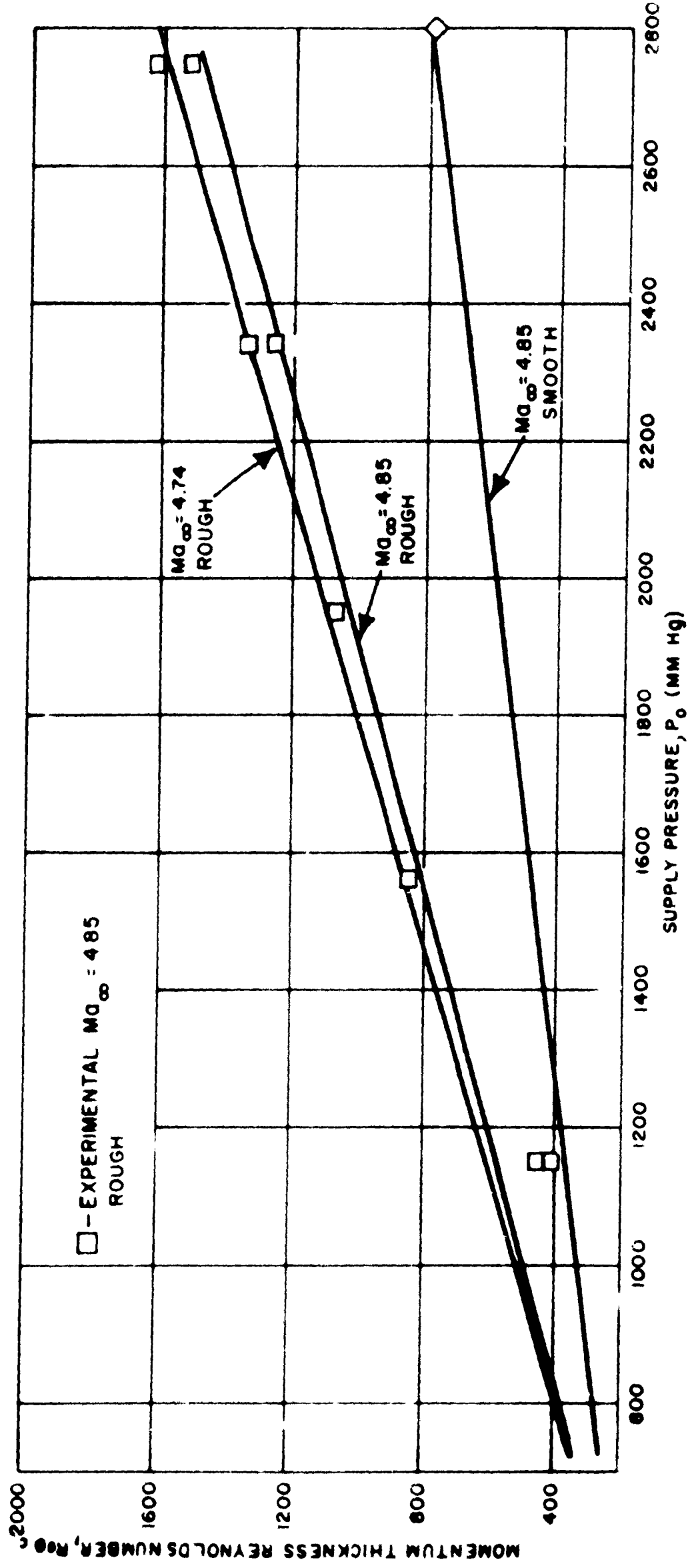


FIG. A6 REYNOLDS NUMBER, $Re_{\theta,c}$, AS A FUNCTION OF SUPPLY PRESSURE FOR THE 10° SPHERE CONE

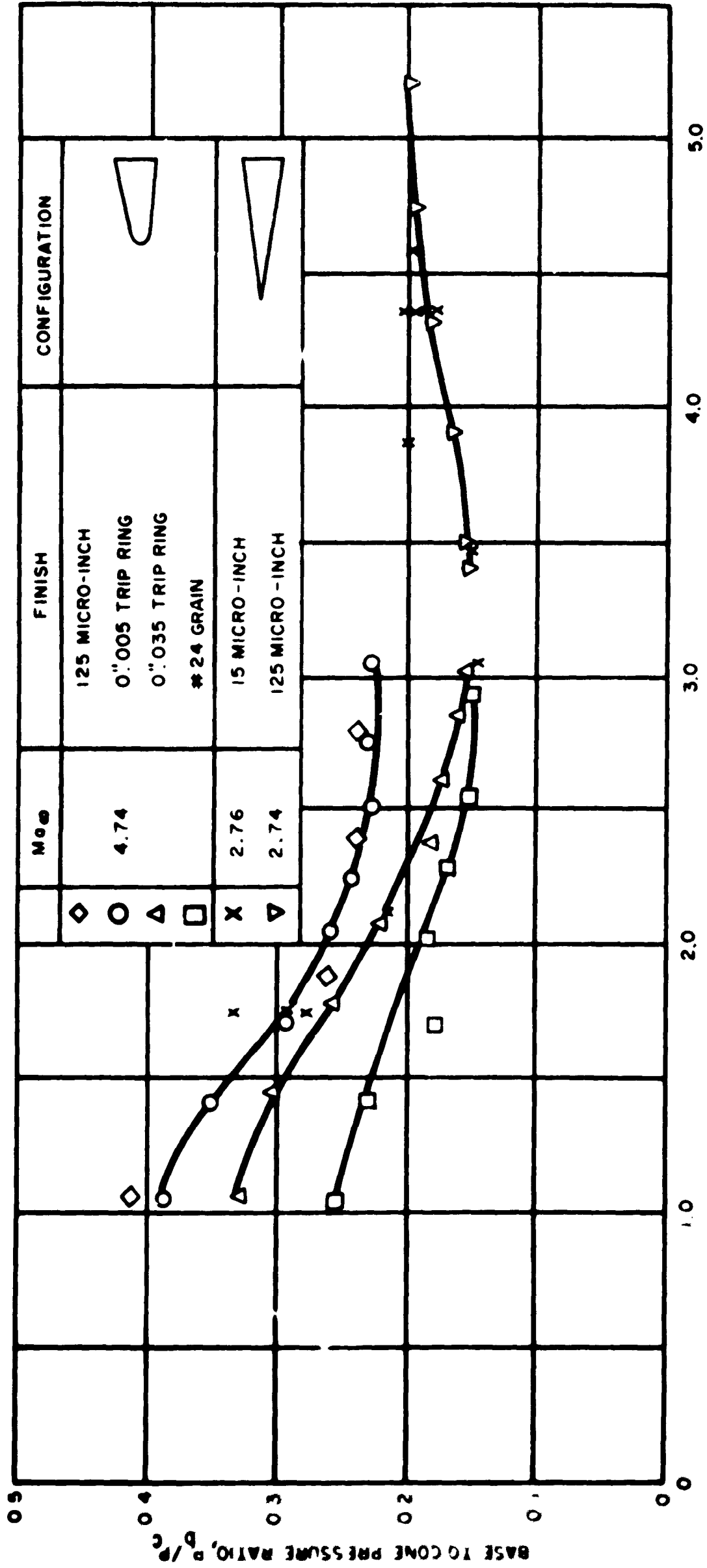


FIG. B1 EFFECT OF SURFACE ROUGHNESS ON BASE PRESSURE